Low-Level Mesovortices within Squall Lines and Bow Echoes. Part II: Their Genesis and Implications

ROBERT J. TRAPP*

Cooperative Institute for Mesoscale Meteorological Studies, University of Oklahoma, Norman, Oklahoma

MORRIS L. WEISMAN

National Center for Atmospheric Research,[+] Boulder, Colorado

ABSTRACT

This two-part study proposes a fundamental explanation of the genesis, structure, and implications of low-level, meso-γ-scale vortices within quasi-linear convective systems (QLCSs) such as squall lines and bow echoes. Such ''mesovortices'' are observed frequently, at times in association with tornadoes.

Idealized experiments with a numerical cloud model show that significant low-level mesovortices develop in simulated QLCSs, especially when the environmental vertical wind shear is above a minimum threshold and when the Coriolis forcing is nonzero. As illustrated by a QLCS simulated in an environment of moderate vertical wind shear, mesovortexgenesis is initiated at low levels by the tilting, in downdrafts, of initially crosswise horizontal baroclinic vorticity. Over a 30-min period, the resultant vortex couplet gives way to a dominant cyclonic vortex as the relative and, more notably, planetary vorticity is stretched vertically; hence, the Coriolis force plays a direct role in the low-level mesovortexgenesis. A downward-directed vertical pressure-gradient force is subsequently induced within the mesovortices, effectively segmenting the previously (nearly) continuous convective line.

In moderate-to-strong environmental shear, the simulated QLCSs evolve into bow echoes with ''straight line'' surface winds found at the bow-echo apex and additionally in association with, and in fact induced by, the low-level mesovortices. Indeed, the mesovortex winds tend to be stronger, more damaging, and expand in area with time owing to a mesovortex amalgamation or ''upscale'' vortex growth. In weaker environmental shear—in which significant low-level mesovortices tend not to form—damaging surface winds are driven by a rear-inflow jet that descends and spreads laterally at the ground, well behind the gust front.

1. Introduction

In this second of a two-part paper, we continue our examination of *low-level* (altitudes below ~1 km AGL), *meso-γ-scale* (horizontal scales ~2–20 km and time-scales ~1 h; Orlanski 1975) vortices, or *mesovortices,* that form at the leading edge of extensive quasi-linear mesoscale convective systems (QLCSs) such as squall lines and bow echoes. The structure and evolution of low-level mesovortices in QLCSs were characterized in Weisman and Trapp (2003, hereafter Part I), as was the range of unidirectional environmental wind profiles

* Current affiliation: Department of Earth and Atmospheric Sciences, Purdue University, West Lafayette, Indiana.
[+] The National Center for Atmospheric Research is sponsored by the National Science Foundation.

Corresponding author address: Dr. Robert J. Trapp, Department of Earth and Atmospheric Sciences, Purdue University, 550 Stadium Mall Drive, West Lafayette, IN 47907.
E-mail: jtrapp@purdue.edu

most conducive to their development. Our focus in Part II is on the genesis of these vortices and then, more generally, on their roles in the convective system structure and evolution.

We recall previous observational (e.g., Smull and Houze 1987; Schmidt and Cotton 1989) and theoretical and/or numerical cloud-modeling studies (e.g., Thorpe et al. 1982; Rotunno et al. 1988; Weisman 1992, 1993) of QLCSs that have focused primarily on convective-system-scale characteristics and how these relate to the longevity, severity, and overall dynamics of the system itself. A particularly relevant characteristic is the *mid-level* (altitudes between ~3 and 7 km AGL) mesovortex pair that forms at the lateral ends of a finite convective system as well as at the ends of embedded bowing segments. These ''book-end'' or ''line-end'' vortices act to focus the rear inflow (hence leading-edge lift, etc.), contributing on the system scale to perhaps as much as 30%–50% of the total rear-inflow strength during the mature phase of the QLCS (Weisman 1993).

The genesis mechanisms of midlevel line-end vortices

have been studied recently by Weisman and Davis (1998, hereafter WD98). WD98 showed that subsystem-scale (~5–10 km diameter) line-end vortices are formed as ambient *crosswise* horizontal vorticity (i.e., $\mathbf{V}_H \perp \boldsymbol{\omega}_H$, where $\mathbf{V}_H$ and $\boldsymbol{\omega}_H$ are the horizontal velocity and vorticity vectors, respectively) is vertically tilted by downdrafts associated with embedded bowing segments. System-scale (approximately tens of kilometers) line-end vortices, on the other hand, are formed primarily through the vertical tilting, by the system-scale updraft, of crosswise horizontal vorticity generated in horizontal buoyancy gradients along the gust front. The development of a larger-scale (approximately hundreds of kilometers) midlevel cyclonic vortex in the stratiform region of an asymmetric convective system owes largely to the stretching of planetary vorticity by mesoscale updrafts (e.g., Bartels and Maddox 1991; Skamarock et al. 1994; WD98).

It is instructive to compare these mechanisms with those that generate mesocyclones in supercell storms. At midlevels, mesocyclones generally develop through the vertical tilting and stretching by the supercell updraft of ambient horizontal vorticity [e.g., see the review by Davies-Jones et al. (2001)]. According to Rotunno and Klemp (1985) [Davies-Jones and Brooks (1993)], mesocyclogenesis at low levels occurs as *streamwise* horizontal vorticity (i.e., $\mathbf{V}_H \parallel \boldsymbol{\omega}_H$), generated primarily in buoyancy gradients along the forward- (rear) flank gust front, and is vertically tilted in the storm's main updraft (rear-flank downdraft). Alternative explanations have been offered in Davies-Jones (2000a) and Wakimoto et al. (1998), the latter involving the release of a horizontal "shearing" or barotropic instability inherent in a zone of concentrated, preexisting vertical vorticity (effectively, a vertical vortex sheet). In brief, such a zone that exists along, say, a gust front becomes unstable and then "rolls" up into discrete, like-signed vortices of uniform, along-front spacing (see Carbone 1983; Lee and Wilhelmson 1997; Mak 2001). This particular mechanism is often used to explain tornadoes and/or their parent vortices within observed squall lines and bow echoes (e.g., Forbes and Wakimoto 1983; Przybylinski 1995).

As demonstrated in Part I, supercell mesocyclones evolve and are structurally quite different than mesovortices in extensive QLCSs. Accordingly, little discussion is devoted hereafter to supercell mesocyclones and, in particular, lines of supercells. Though environments with large vertical wind shear over deep layers— believed to be most often supportive of supercell storm development—are included for completeness in our experimental matrix (see Table 1 of Part I), we concentrate our study on the products of environments of unidirectional vertical wind shear (U_S) over relatively shallow layers (Fig. 3 of Part I) and convective available potential energy (CAPE) of 2200 J kg^{-1}.

For example, in environments with $U_S = 10$ to 15 m s^{-1} over a 2.5- to 5-km depth, an upshear-tilted system results, with relatively weak line-end, system-scale vor-

tices at midlevels (e.g., Figs. 4a,b of Part I). At low levels, only weak, insignificant vortices develop; for our purposes, a "significant" mesovortex is one with a diameter ≥ 4 km (four horizontal grid intervals; nominally resolved), maximum vertical vorticity ≥ 0.01 s^{-1}, vertical depth >1 km, and general time and space coherency. Environments with $U_S = 20$ to 30 m s^{-1}/2.5 to 5 km support the formation of a squall line that develops large bowing segments with significant vortices at mid- and low-levels (Figs. 1, 2). Our objective in Part II is to (i) determine the genesis mechanism of such low-level mesovortices and then (ii) explore their roles in the generation of damaging surface winds and in the evolution and also the structure of the parent QLCS.

2. Experimental methodology

The design of this numerical cloud-modeling experiment is detailed in Part I. Summarizing here, we use the Klemp and Wilhelmson (1978) cloud-resolving numerical model over a domain that is 500 km in the horizontal directions and 17.5 km in the vertical direction. Horizontal gridpoint spacings of 1 km and vertical grid stretching (with 0.3-km gridpoint spacing in the lowest 1 km) are used to represent well the horizontal and vertical structure of the mesovortices. The model is integrated in time to 6 h. All simulations, unless otherwise indicated, include effects of the Coriolis force (assuming a constant f plane, with Coriolis parameter $f = 10^{-4}$ s^{-1}), which is applied only to the wind perturbations.

Sensitivity of low-level QLCS structure to unidirectional environmental wind shear over the range $10 \leq U_S \leq 30$ m s^{-1} over 2.5-, 5.0-, or 7.5-km depths is discussed extensively in Part I. Part II is devoted primarily to analysis of the $U_S = 20$ m s^{-1}/2.5 km experiment (hereafter denoted as 20/2.5/f; an analogous convention is followed for other experiments), the results of which we attempt to generalize to other QLCSs.

3. Overview of the simulation with an environmental shear of $U_S = 20$ m s^{-1} over 2.5 km

Comparable to observed severe convective systems, the QLCS simulated in an environment with $U_S = 20$ m s^{-1}/2.5 km has an evolution and structural characteristics described as follows: Storms triggered initially by the thermal perturbations form rainy downdrafts and associated cold pools whose mutual interaction leads to, after 2 h of model integration, an effectively continuous gust front on the 160-km length scale of the line of initial thermals. Midlevel vortex couplets (Fig. 1a) and also nascent low-level cyclonic mesovortices (Fig. 2a) can be found at this early stage of evolution, characterized by a group of individual cells (e.g., Klimowski et al. 2000). Evident within the resultant squall line at $t = 3$ h are midlevel line-end vortices with
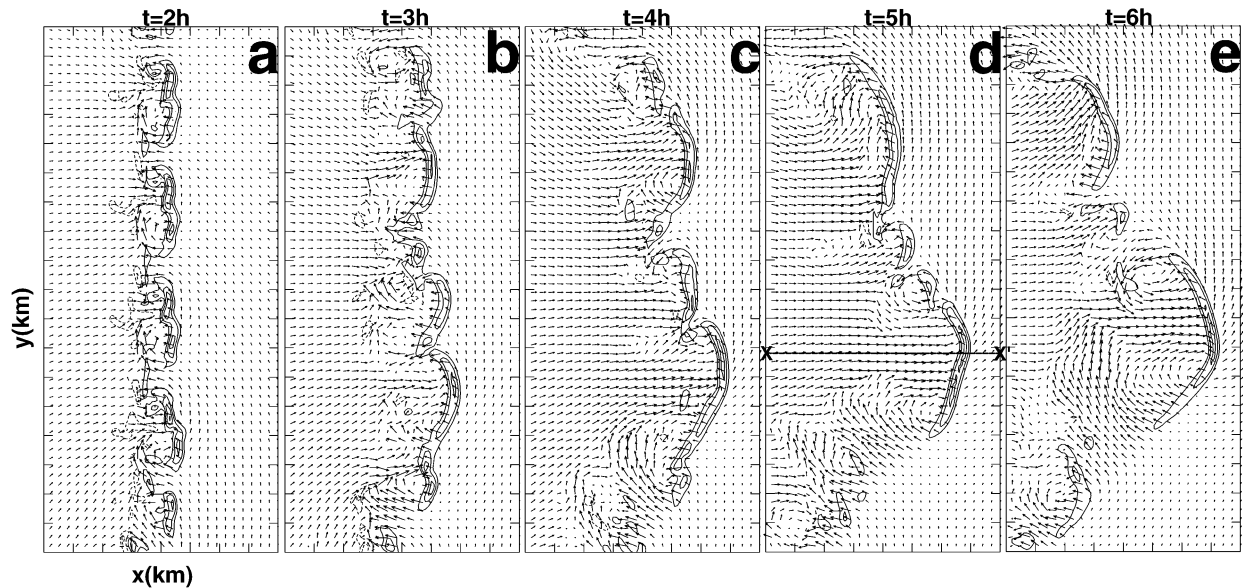
FIG. 1. Horizontal cross section, at $z = 3$ km, of vertical velocity contours and horizontal velocity vectors at (a) $t = 2$ h, (b) $t = 3$ h, (c) $t = 4$ h, (d) $t = 5$ h, and (e) $t = 6$ h. Contour interval is 5 m s^{-1}. Every third vector is plotted, and the vector length is scaled so that a horizontal distance of 3 km represents a speed of 5 m s^{-1}. Tick marks are plotted every 10 km. Unless otherwise indicated, the zero contour is omitted in this and all other plots, dashed contours indicate negative values, and the plotting domain is adjusted so that the moving QLCS is approximately centered within it. Only an 80 km × 180 km portion of the full domain is shown.

diameters of about 15 km and low-level vortices else-where along the line with diameters of 5–10 km (Figs. 1b, 2b). In particular, the cyclonic vortex identified as V1 exemplifies the type of low-level mesovortices of most interest here: it persists for at least 2 h, extends through midlevels, resides in a location just behind the leading edge of the cool air (-1-K isotherm), and

is associated locally with a hook shape in both the model rainwater field and the midlevel updraft (see also Part I).

By $t \geq 4$ h the linear convective system evolves into one with large, outward bowing segments. Attendant with the primary bowing segment are a system-scale midlevel vortex couplet and rear-inflow jet (RIJ; Smull
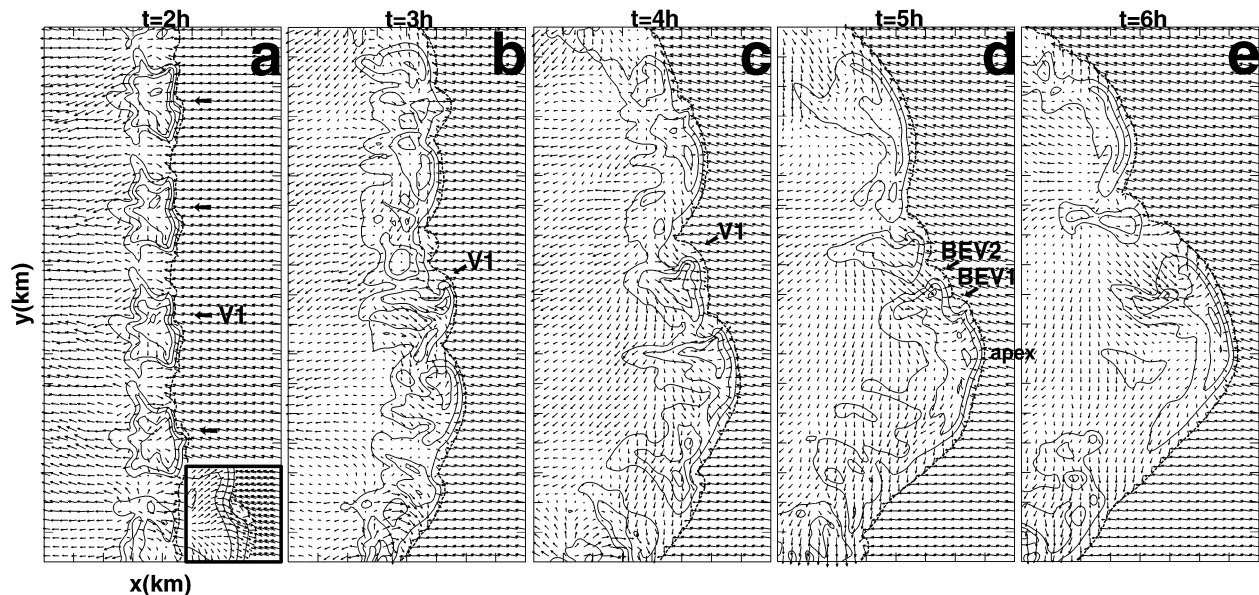

FIG. 2. As in Fig. 1, except with the 1, 3, and 5 g kg^{-1} rainwater mixing ratio contours, at $z = 0.25$ km, and including the -1-K perturbation temperature isotherm (dashed line). Labels and arrows identify features discussed in the text. Inset in (a) shows vortex V1 in a 15 km × 15 km subdomain.
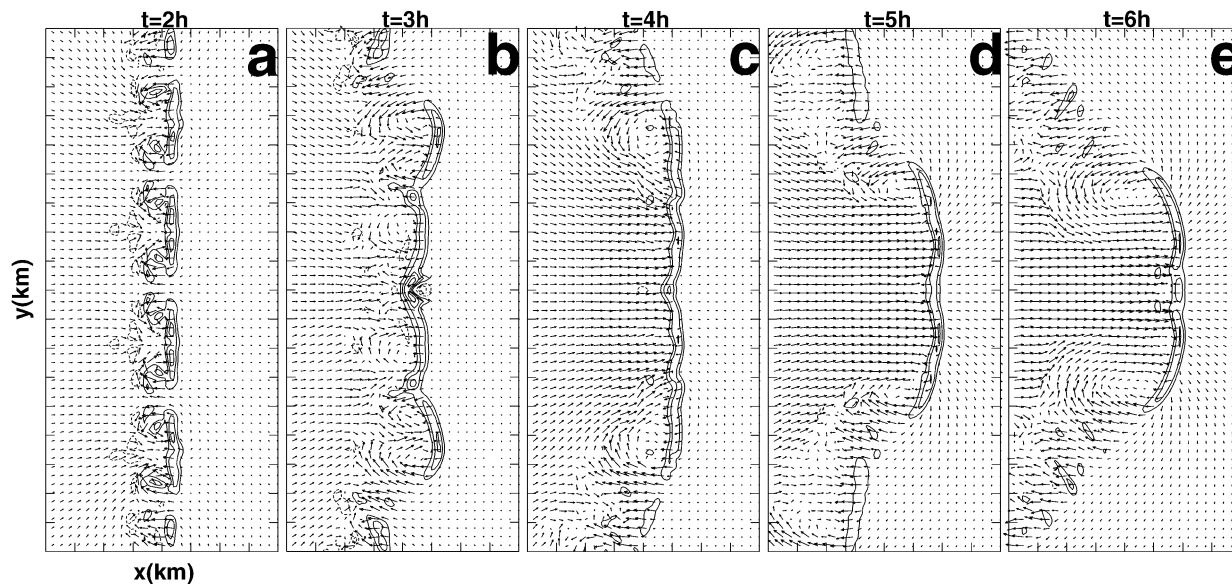
FIG. 3. As in Fig. 1, except for the 20/2.5/0 simulation.

and Houze 1987), the latter extending 40–50 km rearward from the segment's apex (Figs. 1c,e). The RIJ is generally elevated, save for a small branch that descends to low levels just behind the gust front (Figs. 2d,e). The significant low-level cyclonic mesovortices, particularly the one denoted BEV1 (bow-echo vortex 1), are now located exclusively north of the bow apex (Figs. 2c,e). This noteworthy result, consistent at least with tornado observations[1] in bow-shaped convective systems (e.g., Fujita 1979; Przybylinski 1995), elicits two additional findings: 1) a north-of-apex bias in cyclonic vortex location does not exist prior to large bow-segment development and 2) a low-level counterpart to the midlevel *anticyclonic* vortices is generally absent in the simulated QLCS except at the extreme southern end of the system.

A result that is generally *inconsistent* with most bow-echo observations is the location of the *strongest* low-level winds at these later times: tens of kilometers northwest of the apex and in association with low-level mesovortices (see section 5). We regard these as "straight line" winds—in contrast with swirling, tornadic winds that are subgrid scale here—and note that they occur in addition to those found just behind the bow-echo apex, as is typically conceptualized (e.g., Fujita 1978; Przybylinski 1995; Weisman 2001; Wakimoto 2001) (Figs. 2d,e).

The asymmetry of the mature mesoscale convective system (MCS) is also apparent by $t \geq 4$ h. As discussed by Weisman (1993), Skamarock et al. (1994), WD98,

and others, such system-scale asymmetry is promoted through the Coriolis force. Other, more local effects ascribed to Coriolis force can be revealed by comparing the $20/2.5/f$ results with those from a counterpart simulation with f set to zero ($20/2.5/0$) (Figs. 3, 4). Indeed, although at $t = 2$ h the midlevel vortex structure in both cases is nearly identical, as are many other facets of the motion and precipitation fields (see, e.g., Figs. 1a, 3a), significant low-level mesovortices are conspicuously absent in the $f = 0$ case (Fig. 4a). The low-level wind field is free of vortices at later times as well (Figs. 4b–e), suggesting a probable link between mesovortexgenesis and f, explored in the next section. Yet another apparent effect of f regards the midlevel updraft. At $t > 3$ h in the $20/2.5/0$ simulation, we find that the midlevel updraft becomes rather uniform horizontally (Figs. 3c–e), lacking the segments and subsystem-scale vortices observed at these times in the $20/2.5/f$ simulation (Figs. 1c–e). As discussed in section 6, such segmentation is related to the presence of low-level mesovortices and hence can be viewed as a secondary effect of f.

4. Analysis of low-level mesovortexgenesis

The development of a prominent low-level vortex such as V1 is now examined. Vortex V1 is one of at least four leading-edge mesovortices that are well formed by $t = 2$ h. At this nascent stage of the modeled QLCS, low-level vortexgenesis is disclosed more readily because the convective system is still symmetrical and, in this regard, less complicated structurally than at later stages. Our knowledge of V1's formation, however, is used later in this section to explain vortexgenesis within a mature QLCS with large bowing segments.

---

[1] Exceptions can be found in Wakimoto (1983), who reported an F4 (Fujita 1981) *anticyclonic* tornado that developed within the cyclonically rotating comma head of a bow echo, and also in Forbes and Wakimoto (1983), who showed that 9 of the 18 tornadoes that occurred on 6 August 1977 in central Illinois developed south of the bow-echo apex; these 9 tornadoes were rated F1 or below.
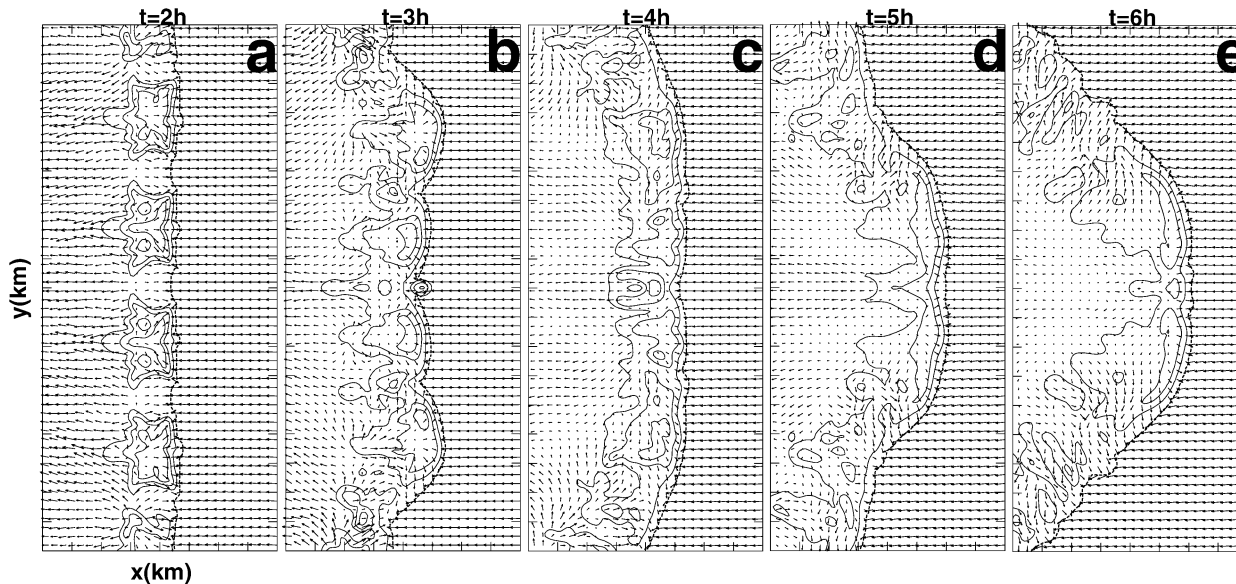
FIG. 4. As in Fig. 2, except for the 20/2.5/0 simulation.

a. Early-stage vortexgenesis

The developmental history of V1 (and of the other early-stage vortices) can be traced back to at least $t = 1$ h 20 min. At this time, V1 is the cyclonic member of a symmetrical cyclonic–anticyclonic vortex couplet that straddles a low-level downdraft and rainwater maximum (Fig. 5a); the downdraft originates at midlevels, in conjunction with a short-lived cell split. Thereafter, the couplet separates owing to outflow expansion and subsequent updraft and downdraft evolution. Vortex V1 continues to intensify, while its anticyclonic counterpart experiences very little growth (Fig. 5b). Figure 5 suggests the need to determine (i) the process(es) responsible for the formation of the low-level vortex couplet and then (ii) the means by which the symmetry in the vortex couplet's development is broken. An obvious clue to (ii) is immediately provided by the 20/2.5/0 simulation: A low-level vortex couplet is generated by $t = 1$ h 20 min yet, in contrast to the couplet in 20/2.5/f, remains symmetrical and weak through $t = 1$ h 40 min (Figs. 5c,d).

1) VERTICAL VORTICITY EQUATION ANALYSIS

Consider the vertical vorticity equation formed from the model equations, which can be written as follows:

$$\frac{d\zeta_a}{dt} \equiv \frac{\partial \zeta_a}{\partial t} + \mathbf{V}_H \cdot \mathbf{\nabla}_H \zeta_a + w \frac{\partial \zeta_a}{\partial z}$$
$$= \boldsymbol{\omega}_H \cdot \mathbf{\nabla}_H w - \zeta_a \mathbf{\nabla}_H \cdot \mathbf{V}_H + \mathbf{\nabla}_H \cdot \mathbf{D}, \quad (4.1)$$

where $\zeta_a = \zeta + f$ is absolute vertical vorticity, $\mathbf{D} = D_v \hat{\imath} + (-D_u)\hat{\jmath}$ composes the eddy-mixing terms from the horizontal momentum equations, $\mathbf{\nabla}_H$ is the horizontal gradient operator, and $\mathbf{V}_H$ and $\boldsymbol{\omega}_H$ are the horizontal

velocity and vorticity vectors, respectively. The rhs terms in Eq. (4.1) govern vertical tilting of horizontal vorticity, stretching of planetary plus relative vertical vorticity, and eddy mixing of absolute vertical vorticity, respectively. We examine these forcing terms in perhaps the most familiar of the two complementary approaches taken herein to reveal the vortexgenesis mechanism.

We begin with a consideration of the 20/2.5/0 simulation, which represents the simplest or most idealized case, since the solution is inherently symmetrical and also mirrors the 20/2.5/f solution through ~1 h 20 min (Fig. 5). Using plots of horizontal vorticity and vertical velocity, one can deduce that the generating mechanism of the low-level vortex couplet is simply the tilting of initially crosswise horizontal vorticity in a downdraft. Indeed, Fig. 6 depicts a horizontal vortex ring that was baroclinically generated in cold-air outflow from a prior downdraft, then expanded, and now passes in part through the core of a new downdraft. Tilting of the horizontal vorticity generates cyclonic vertical vorticity south of the downdraft core and anticyclonic vertical vorticity north of the core.

The tilting process can be quantified by a time integration of relevant ζ-forcing terms along a backward trajectory, originating at $t = 1$ h 20 min within the $z = 0.4$ km ζ_{max} (Fig. 6); trajectory calculations are performed using 1-min history files. Figure 7 proves that most of the ζ generated by $t = 1$ h 20 min is through the tilting of horizontal vorticity in *descending* air (i.e., after $t \sim 1$ h 15 min along the trajectories). As substantiated by the buoyancy field in Fig. 6, such horizontal vorticity is primarily baroclinic (i.e., horizontal vorticity vectors are parallel to buoyancy contours), while horizontal vorticity tilted in *rising* air along the trajectories (i.e., prior to $t \sim 1$ h 15 min) is barotropic
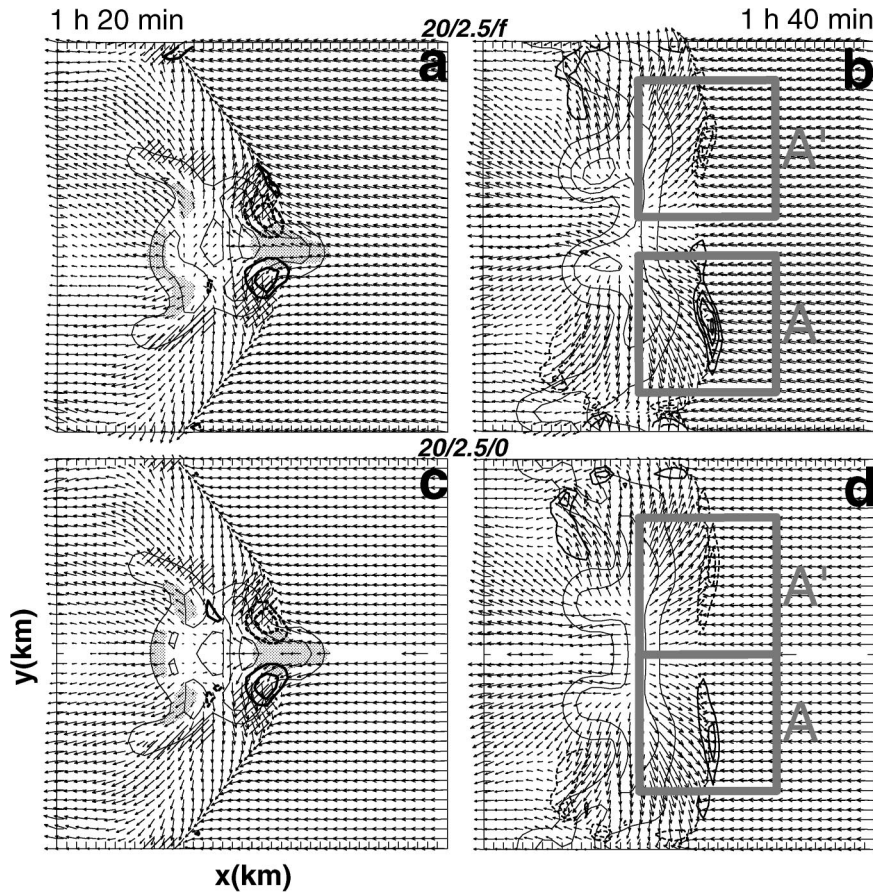
FIG. 5. Horizontal velocity vectors, the 1, 3, and 5 g kg^{-1} rainwater contours (thin lines), and vertical vorticity contours (bold lines; contour interval of 0.004 s^{-1}) at $z = 0.4$ km. (a), (b) The 20/2.5/f simulation at $t = 1$ h 20 min and 1 h 40 min, respectively. (c), (d) The 20/2.5/0 simulation at $t = 1$ h 20 min and 1 h 40 min, respectively. The vector length is scaled so that a horizontal distance of 1 km represents a speed of 10 m s^{-1}. In (a) and (d), the stippled regions enclose vertical velocities less than or equal to -5 m s^{-1} at $z = 3$ km, and the hatched regions enclose vertical velocities greater than or equal to 10 m s^{-1} at $z = 3$ km. In (b) and (d), the gray boxes represent control areas A and A' (see text). Only a 40 km $\times$ 40 km portion of the full domain is shown.

or due to the environmental wind shear (see Dutton 1986, 389–390). Note that in the descending air parcels, negative (positive) stretching of relative vertical vorticity counteracts the positive (negative) tilting of baroclinic horizontal vorticity.

The mechanism that breaks the symmetry of the vortex couplet and hence leads to a dominant cyclonic vortex involves planetary vorticity, as evidenced by the disparity between the 20/2.5/f and 20/2.5/0 experimental results (Figs. 8a,b). An even greater disparity exists between the 20/2.5/0 solution and one from an experiment with $f = 2 \times 10^{-4}$ s^{-1} (20/2.5/2f; Fig. 8c). The 20/2.5/2f equivalent of V1 has developed more rapidly and is larger in scale at 2 h than V1; generally speaking, this holds true at all times for this and other low-level mesovortices in the 20/2.5/2f experiment (not shown). Though admittedly an unrealistic experiment (f actually ranges from 0 at the equator to $\pm 1.46 \times 10^{-4}$ s^{-1} at

the two poles), such a clear model response to a doubling in Coriolis parameter value suggests to us a direct effect of f on the mesovortexgenesis, which we now explore.

Recall that f enters Eq. (4.1) through the vertical stretching of planetary vorticity. To estimate the magnitude of this process in the simulated QLCS, we examine a parcel's vertical vorticity growth along a *forward* trajectory, originating again at 1 h 20 min within the $z = 0.4$ km ζ_{max} (see Fig. 6); note that along this trajectory, the parcel exits the downdraft and then enters and rises in the leading-edge updraft. The parcel is initialized with $\zeta_0 = f = 10^{-4}$ s^{-1}, which is allowed to grow only through vertical stretching along the trajectory, but does not interact with the surrounding flow. As thus governed [see Eq. (4.1)] by

$$\zeta(t) = \zeta(t_0) \exp\left(\int_{t_0}^{t} - \boldsymbol{\nabla}_H \cdot \mathbf{V}_H \, dt'\right), \qquad (4.2)$$
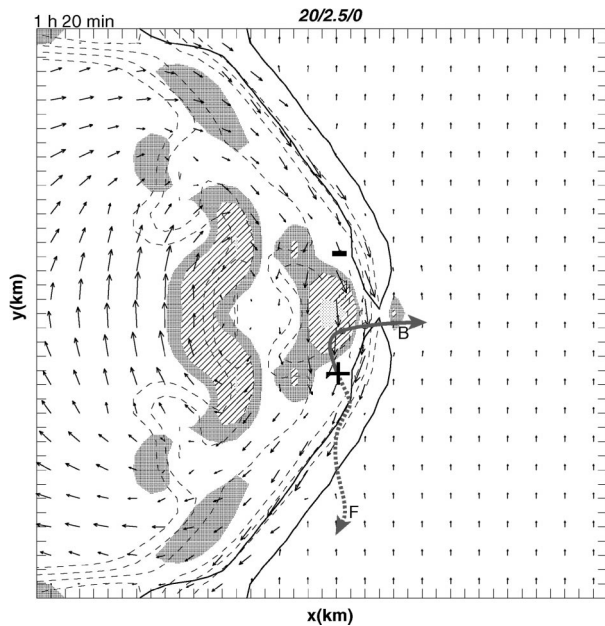
FIG. 6. Horizontal vorticity vectors and vertical velocity at $z = 0.4$ km and $t = 1$ h 20 min and buoyancy at $z = 0.4$ km and $t = 1$ h 15 min. Every second vector is plotted, and the vector length is scaled so that a horizontal distance of 2 km represents a vorticity magnitude of 0.02 s^{-1}. Vertical velocity equal to 1 m s^{-1} is contoured with a solid black line, values less than -4 m s^{-1} have light shading, values between -2 and -4 are hatched, and values between -2 and -1 have dark shading. Buoyancy contour interval is 300×10^{-4} m s^{-2}. Backward trajectory of the parcel originating at 1 h 20 min is represented as a bold gray line, and the forward trajectory originating at 1 h 20 min is represented as a broken gray line. The locations of the vertical vorticity maximum and minimum at 1 h 20 min are indicated by "+" and "−," respectively. Only a 40 km × 40 km portion of the full domain is shown.

FIG. 7. Time series of parcel height (z; km), vertical vorticity (ζ; s^{-1}), and the time-integrated contributions to vertical vorticity from the tilting and relative vorticity-stretching terms [s^{-1}; see Eq. (4.1)], along the backward trajectory denoted as "B" in Fig. 6. The sum of the tilting and stretching terms is plotted as ζ_{sum}.

vertical vorticity along the trajectory increases from an initial value of 1×10^{-4} s^{-1} at 1 h 20 min (and $z = 0.4$ km) to 153×10^{-4} s^{-1} at 1 h 50 min (and $z = 5.8$ km) (Fig. 9)! Strictly speaking, this parcel's vertical vorticity at $t = 1$ h 50 min cannot be qualified as "low level." However, a local or Eulerian application of Eq. (4.2) at low levels, using representative values of horizontal convergence ($\sim -1 \times 10^{-3}$ to -5×10^{-3} s^{-1}), yields comparable magnitudes of vertical vorticity over the 30-min period. Either way, the implication here is that *vertical stretching of initial vertical vorticity equivalent to midlatitude f can significantly enhance the cyclonic vortex and significantly diminish the anticyclonic vortex.*

2) CIRCULATION EQUATION ANALYSIS

We now turn to the circulation equation for an alternative perspective and, ultimately, for confirmation of the conclusions made thus far on the vortexgenesis mechanism. Herein we consider circulation in an Eulerian framework rather than analyzing circulation about a material curve (e.g., Rotunno and Klemp 1985; Da-
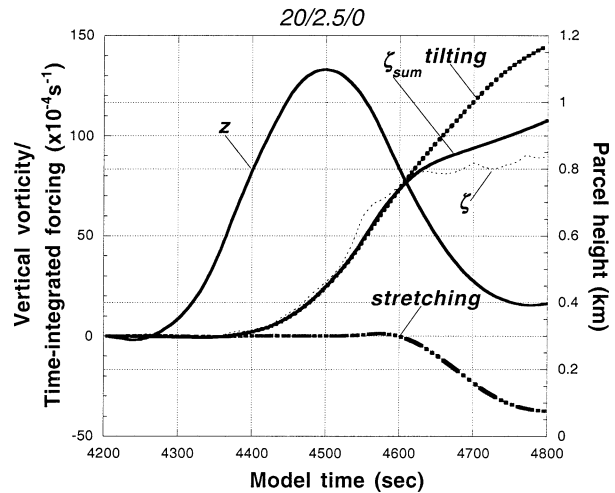
vies-Jones and Brooks 1993; Trapp and Fiedler 1995) that, in the present case, becomes topologically too deformed to afford accurate evaluation of the circulation forcing terms [see, e.g., Eq. (2) of Skamarock et al. (1994)].

We begin with the absolute vertical vorticity equation, now written as

$$\frac{\partial \zeta_a}{\partial t} = \boldsymbol{\nabla}_H \cdot (-\zeta_a \mathbf{V}_H + w \boldsymbol{\omega}_H + \mathbf{D}). \qquad (4.3)$$

Integrating Eq. (4.3) over horizontal control area A (that is held fixed to the grid) and then applying the divergence theorem gives

$$\frac{\partial C}{\partial t} = \frac{\partial}{\partial t} \int \zeta_a \, dA$$

$$= \oint (-\zeta \mathbf{V}_H - f \mathbf{V}_H + w \boldsymbol{\omega}_H + \mathbf{D}) \cdot \hat{n} \, dl, \qquad (4.4)$$

where the line integral is about A, assuming outward unit normal $\hat{n}$. Equation (4.4) describes the absolute[2] circulation tendency, whose forcing terms hereafter are referred to as ζ flux, f flux, ω flux, and mixing, respectively. An illustration of how these terms (less mixing) contribute to positive circulation tendency is provided in Fig. 10.

We note that one advantage of this analysis approach is that it reveals the macroscopic properties of vortexgenesis without the need to choose a "representative" trajectory, as in the preceding Lagrangian analysis of

---

[2] We consider absolute circulation out of notational simplicity and because it differs from relative circulation by a constant; that is, $C_{\mathrm{rel}} = C - fA$, where, in the analysis of V1, $fA = \mathrm{const} = 0.14 \times 10^{5}$.
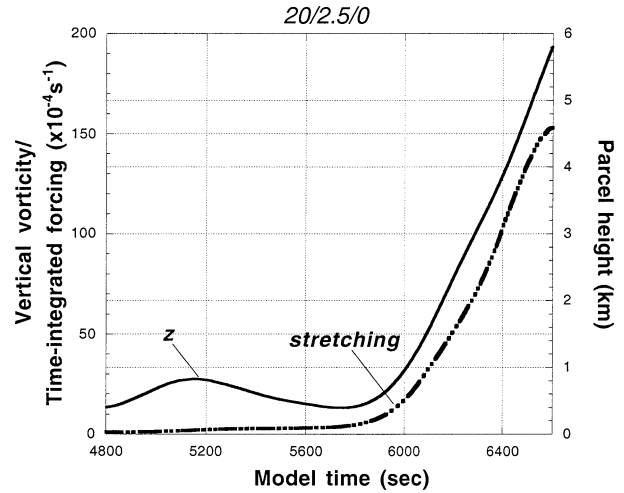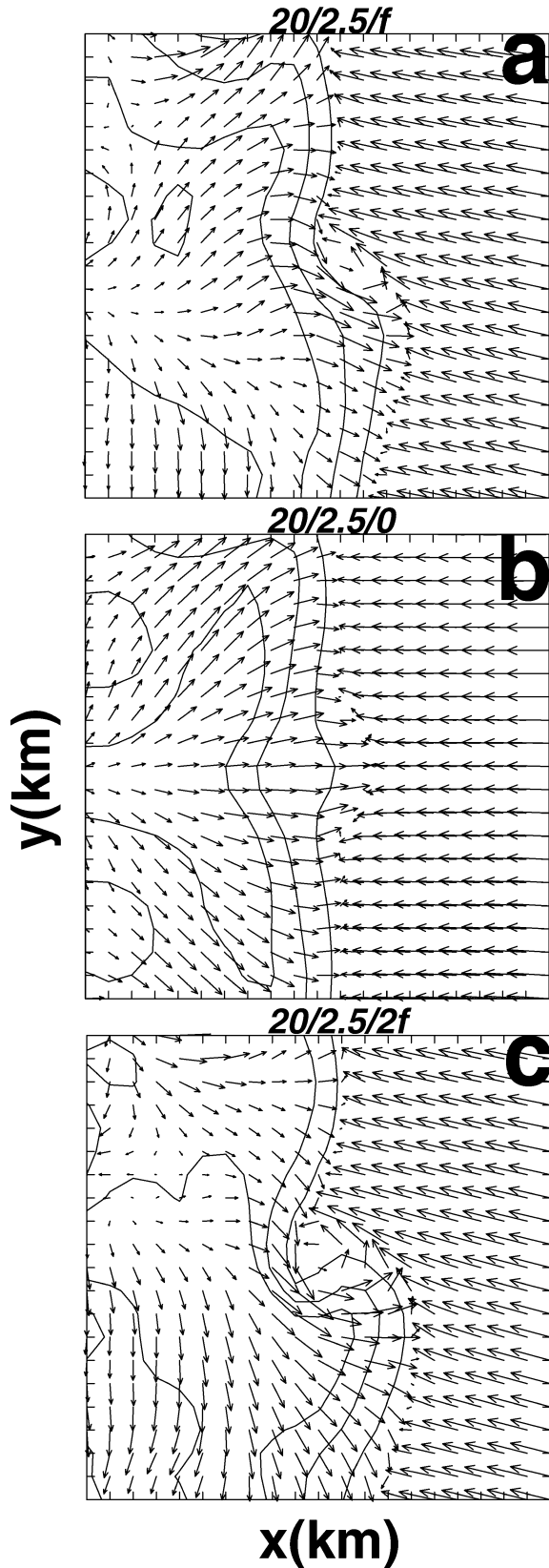
FIG. 9. Time series of parcel height (z; km) and time-integrated contribution to vertical vorticity from the relative vorticity-stretching term [s^{-1}; see Eq. (4.1)], along the forward trajectory denoted as "F" in Fig. 6.

Eq. (4.1). We now apply Eq. (4.4) to the 20/2.5/0 simulation, as done before. Horizontal control areas at $z = 0.4$ km (the second grid level above the ground) are used for the line integrations. These 14 km × 14 km areas A and A' enclose the respective cyclonic and anticyclonic members of the low-level vortex couplet during a 30-min period (1 h 20 min to 1 h 50 min) of the couplet's initial growth (see Fig. 5). Line-integrated forcing terms in Eq. (4.4) are time integrated over this interval as $C(t)_{\omega-\text{flux,etc.}} = \int_{t_0}^{t} (\omega \text{ flux, etc.}) \, dt'$ and then compared with the time series of circulation.

For the purposes of this initial, idealized application, we disregard contributions from mixing and the horizontal flux of relative vorticity and focus solely on circulation generation in the absence of preexisting relative circulation/vertical vorticity. In doing so, the Eulerian circulation perspective shows us first of all that the low-level vortex couplet is generated through a large ω flux (ω' flux) that contributes positively (negatively) to circulation C (C') (Fig. 11). Such $|\omega \text{ flux}|$ arises primarily from the depression of southward-oriented horizontal vortex lines along the north (south) boundary of area A (A') (see Figs. 6, 5c,d), which is consistent with the previously arrived conclusion of couplet formation through horizontal vortex-line tilting.

Also consistent is the symmetry-breaking mechanism, which in the Eulerian circulation analysis is through the f-flux term. The time-integrated effect of

←

FIG. 8. Horizontal velocity vectors and the 1, 3, and 5 g kg^{-1} rainwater contours, at $z = 0.25$ km and $t = 2$ h, for the (a) 20/2.5/f, (b) 20/2.5/0, and (c) 20/2.5/2f simulations. The vector length is scaled so that a horizontal distance of 1 km represents a speed of 10 m s^{-1}. Only a 20 km × 20 km portion of the full domain is shown.

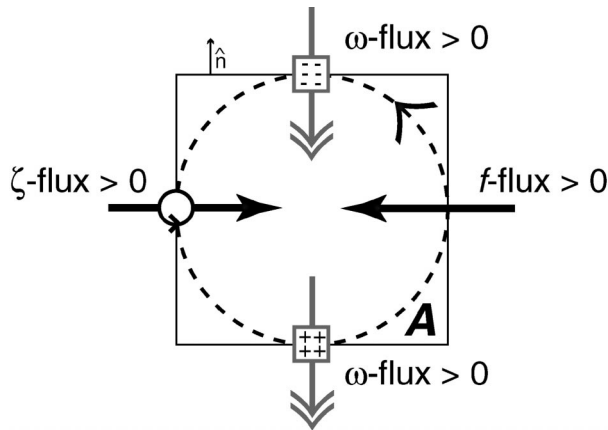FIG. 10. Schematic showing how the ζ flux, f flux, and ω flux terms of Eq. (4.4) may contribute to positive circulation tendency, as represented by the dashed circle. Double-arrowed lines denote horizontal vorticity vectors, and single-arrowed lines denote horizontal velocity vectors. In boxes along the north and south boundaries of A, "$+$" and "$-$" indicate updraft and downdraft, respectively.

this term can be quantified in this $f = 0$ case by computing a "hypothetical" f flux, using the actual $\oint - \mathbf{V}_H \cdot \hat{n}\, dl$ but with $f = 10^{-4}$ s^{-1} instead of $f = 0$ s^{-1}. Note from Fig. 11 that this hypothetical flux of planetary vorticity into the control areas would act to increase circulation monotonically, owing to consistent inflow through both the eastern and western boundaries of A and A'. Indeed, over a 30-min interval, the time-integrated magnitude of the hypothetical f flux is just slightly less than that of the $|\omega$ flux$|$. This result suggests to us that positive f flux into area A' (A) should help mitigate negative (enhance positive) circulation gained
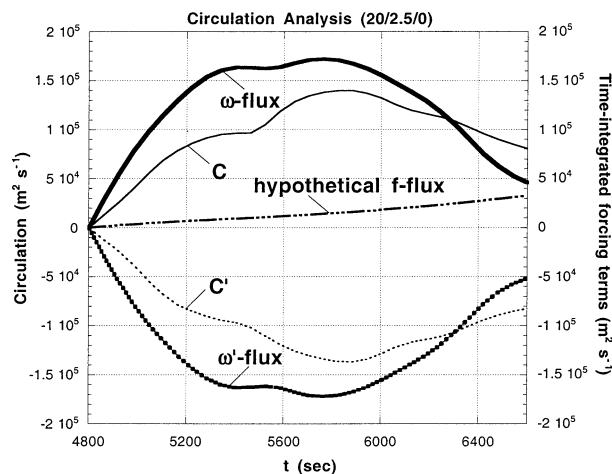

FIG. 11. Time series of circulation C and time-integrated contribution to circulation from the ω flux and from a hypothetical f flux [see Eq. (4.4) and text] for the 20/2.5/0 simulation. Primed variables are relevant for area A'. Source-term calculations are performed at $z = 0.4$ km, with respect to the control areas A and A' (see Fig. 5d), and integrated over the time interval 1 h 20 min $\leq t \leq$ 1 h 50 min. Circulation computed at 1 h 20 min is subtracted from the circulation time series.

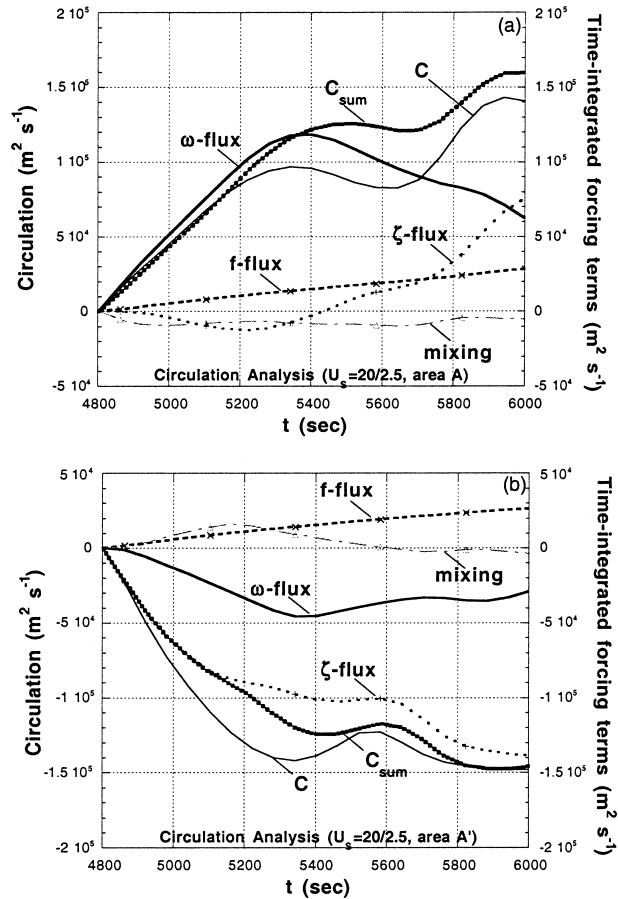

FIG. 12. As in Fig. 11, except for *all* terms in Eq. (4.4) and for the 20/2.5/f simulation. The sum of the time-integrated terms is identified as C_{sum}. Source-term calculations are performed at $z = 0.4$ km, with respect to the control areas (a) A and (b) A' (see Fig. 5b), and integrated over the time interval 1 h 20 min $\leq t \leq$ 1 h 40 min.

by the ω' flux (ω flux) and thereby preclude (allow) the development of an anticyclonic (cyclonic) mesovortex near the ground.

A circulation analysis of the 20/2.5/f simulation, which includes all terms in Eq. (4.4), confirms this basic result of the preceding exercise (Fig. 12). Note that the sizeable contribution to positive and negative circulation, respectively, from the flux of relative vorticity into/out of areas A and A' is explained in part by relative vorticity generated outside the control areas and in part as a consequence or artifact of fixed control areas and a northeasterly storm-motion vector.[3]

Some final calculations are offered to emphasize further the direct role of planetary vorticity in the low-level mesovortexgenesis. As developed in Davies-Jones (1986, 216–217), an equation that governs the cross-sectional

---

[3] For example, $\pm\zeta$ initially generated inside a control area but moving with the storm may later be located along the area boundary and then fluxed back into/out of the area.

area $a(t)$ of a vortex tube in an inviscid, barotropic fluid can be derived from Eq. (4.1) and expressed as

$$\frac{1}{a(t)} \frac{da(t)}{dt} = \delta. \qquad (4.5)$$

Area a of the vortex tube will contract/expand given some constant horizontal divergence δ within a. By virtue of the assumptions above, circulation C about the vortex is constant. Hence, we can initially let $a(0) = C/\zeta_0$. At a later time τ when the vortex core radius has contracted/expanded to r_c, the cross-sectional area is $a(\tau) = \pi r_c^2$. Integrating (4.5) over the interval $0 \leq t \leq \tau$ and then solving for τ gives

$$\tau = \frac{1}{-\delta} \ln\left(\frac{C}{\zeta_0 \pi r_c^2}\right). \qquad (4.6)$$

Applied to our low-level mesovortex problem, Eq. (4.6) yields $\tau = 65$ min given $\delta = -1 \times 10^{-3}$, $r_c = 2.5$ km, $C = 1 \times 10^5$, and $\zeta_0 = f = 1 \times 10^{-4}$. Thus, this simple model shows that planetary vorticity *alone* can be concentrated into a mesovortex in roughly 1 h. We note that calculations by Lilly (1976) also support this statement, even though his were used to explain the development of supercell mesocyclones and tornadoes. Of course, strong, low-level mesocyclones form routinely in supercells simulated with $f = 0$ (e.g., Klemp and Rotunno 1983; Wicker and Wilhelmson 1995), as mechanisms internal to supercells are at least sufficient for mesocyclogenesis; as just demonstrated, strong, low-level mesovortices only form in QLCSs simulated with $f \neq 0$.

b. Generalization of genesis mechanism

Vortexgenesis within a mature QLCS with large bowing segments can be illustrated through an analysis of BEV1, an archetypal north-of-apex vortex (Fig. 13). BEV1's origin as weak horizontal shear along the gust front can be traced back in time, unambiguously, to at least $t = 4$ h 40 min. Hence, we consider the circulation about a 16 km $\times$ 16 km control area α (see Fig. 13) that encloses the developing vortex during the interval 4 h 10 min $\leq t \leq$ 4 h 40 min. Over this 30-min period, C and the time-integrated ζ flux, f flux, and ω flux increase gradually (Fig. 14). At this mature stage, the ζ flux is not dismissed as an analysis artifact but rather is ascribed in part to broad-scale relative vorticity well behind the leading edge (see below). Enhancing this contribution and that from the ω flux to positive circulation is again the flux of planetary vorticity. And, owing to the positive f flux into area α' (see Fig. 13), which mitigates negative circulation gained by negative ω flux, the development of a symmetric vortex pair near the ground is again unrealized (Fig. 14b).

BEV1's genesis is in essence the same as that of V1 from the vorticity equation perspective, with one exception: BEV1 also benefits from the horizontal advec-
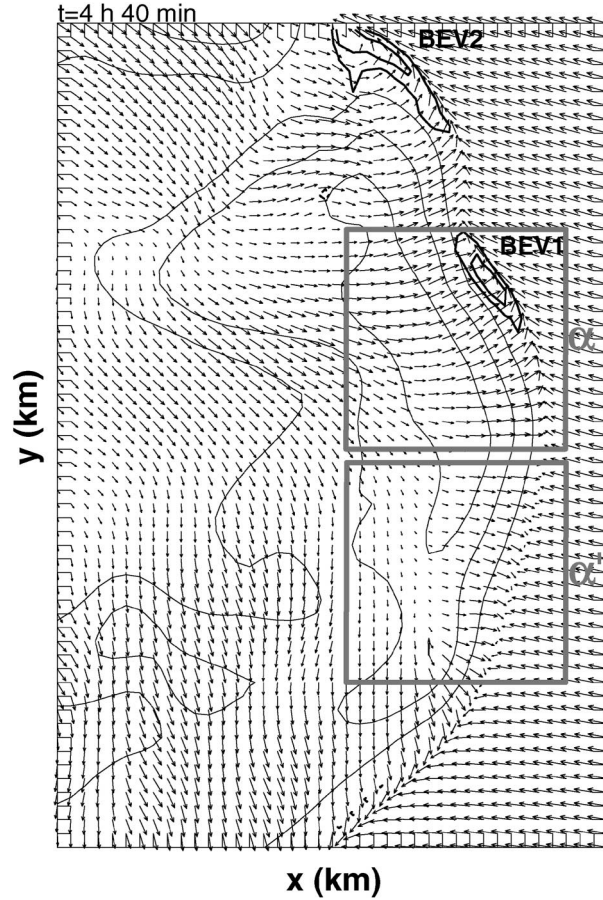

FIG. 13. As in Fig. 5, except at $t = 4$ h 40 min. The gray boxes denote control areas α and α'. Only a 40 km $\times$ 60 km portion of the full domain is shown.

tion (not shown) of weak, broader-scale relative vorticity toward the system's leading edge, as can be visualized in the wind field in Fig. 13. Note that in the real atmosphere, we would expect such residual/larger-scale ζ to be present in some form even before cumulus convection is initiated and, hence, contribute to early-stage vortexgenesis as well. The larger-scale ζ as well as ζ generated in situ is due as before to tilting, in a low-level downdraft, of horizontal vorticity and then to the vertical stretching of relative and planetary vertical vorticity. The details of the tilting process are, however, different than before, owing to differences in the overall QLCS structure at this stage. Specifically, the horizontal vorticity now is that due to the vertical shear beneath the RIJ core (Fig. 15), although $\boldsymbol{\omega}_H$ is still predominantly crosswise and also baroclinic (Lafore and Moncrieff 1989; Weisman 1992); the downdraft is now much broader and resides several kilometers behind the leading-edge updraft (Fig. 15). These two components of vortexgenesis have been recognized by Davies-Jones (2000b) and idealized in his analytic model. His model neglects the earth's rotation, however, and thus it does
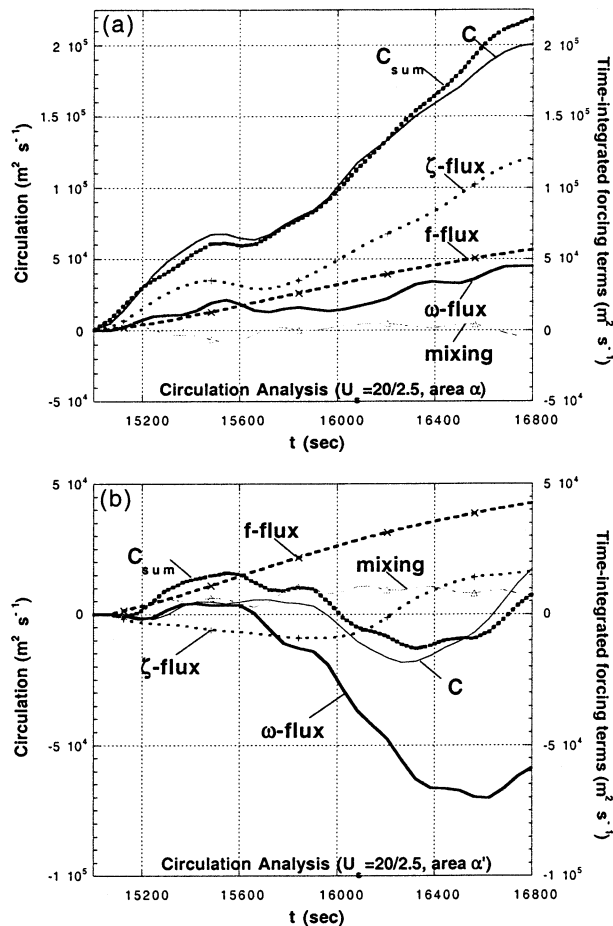
FIG. 14. As in Fig. 12, except for (a) control area α and (b) control area α' (see Fig. 13), integrated over the time interval 4 h 10 min $\leq t \leq$ 4 h 40 min. Circulation computed at $t =$ 4 h 10 min is subtracted from the circulation time series.

FIG. 15. West–east vertical cross section through the apex of the primary bowing segment at $t =$ 4 h 10 min. Contours are of vertical velocity (-0.5, 1, 5, and 10 m s^{-1}). The stippled regions enclose y-component horizontal vorticity between 50 and 150 $\times$ 10^{-4} s^{-1} and the hatched regions enclose y-component horizontal vorticity greater than 150 $\times$ 10^{-4} s^{-1}. Vectors are of velocity in the x–z plane. Every second vector is plotted, and the vector length is scaled so that a distance of two grid lengths in the horizontal or vertical represents a vector magnitude of 15 m s^{-1}. The horizontal (vertical) subdomain is 30 km (15 km).

not explain the predominance of a cyclonic mesovortex at low levels in the bow-echo case.

A variation has just been demonstrated in the details of the mechanism of significant, low-level mesovortices within a *specific* simulated QLCS. Results from Part I and additional analyses of the experiments presented therein (not shown) suggest that low-level mesovortexgenesis likewise varies in detail over a range of QLCS configuration/structure and hence environmental shear. However, the general process of initial generation through tilting of horizontal crosswise vorticity, followed by amplification into significant mesovortices through stretching of relative and planetary vorticity, is consistent throughout all relevant modeled convective systems.

c. Comments on shearing instability mechanism

Not mentioned thus far is the so-called horizontal shearing or barotropic instability mechanism of vortexgenesis. As noted in section 1, this particular mechanism
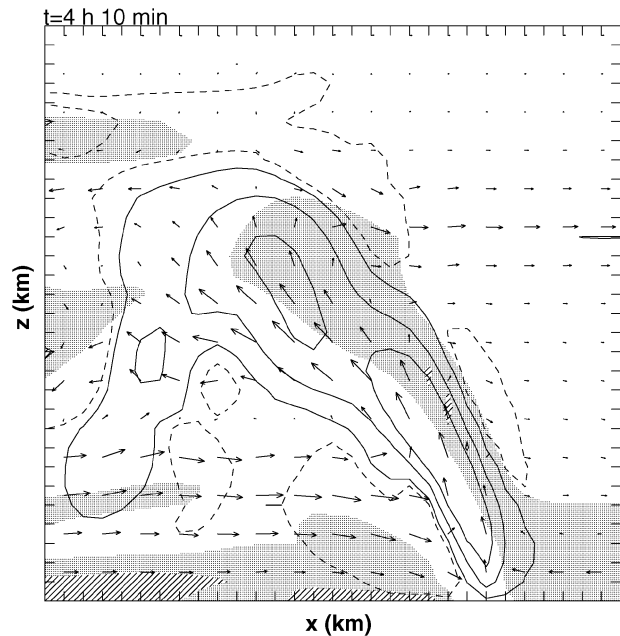
has been used frequently to explain observations of tornadoes and/or their parent vortices within squall lines and bow echoes (e.g., Forbes and Wakimoto 1983; Przybylinski 1995). Using idealized numerical model simulations, Lee and Wilhemlson (1997) have demonstrated that the release of a horizontal shearing instability can be responsible for nonsupercell tornadogenesis.

Consider a time sequence of the low-level ζ field in the 20/2.5/f simulation (Fig. 8 of Part I). In contrast to the nonsupercell tornadogenesis case, in which an unstable vertical vortex sheet "rolls" up into discrete, *like-signed* vortices (e.g., Fig. 9 of Lee and Wilhelmson 1997) we find in our QLCS cases an early ζ field characterized by vortex *couplets*. Thus, consistent with the analysis presented above, low-level vortices during the early QLCS stages clearly do not form as part of the release of horizontal shearing instability (see also Fig. 13 of Part I). Furthermore, most of the low-level mesovortices at t = 5 h and beyond can be traced directly back to the cyclonic member (or at least its remnant) of an initial couplet; it follows that these mesovortices in the mature QLCS also do not form via the release of horizontal shearing instability. The foregoing statements apply strictly to our modeled QLCSs, which were initiated in a horizontally homogeneous environment that is by definition free of initial (relative) horizontal shear. In the
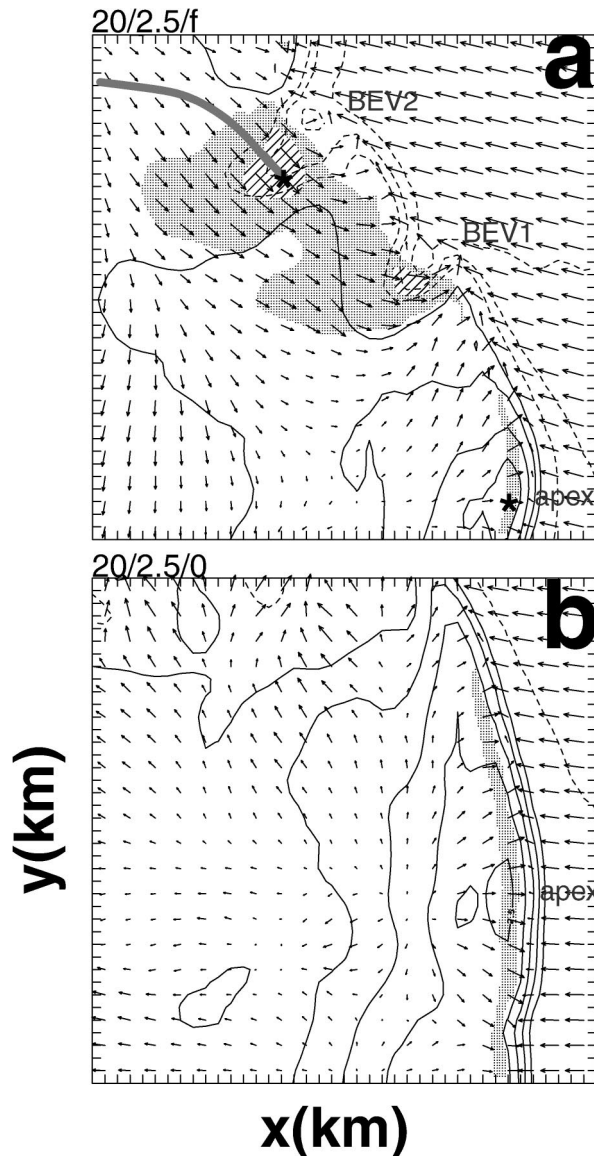
FIG. 17. Ground-relative horizontal wind magnitude (bold dark lines, 35 m s^{-1} contour; thin dashed line, 40 m s^{-1} contour) at $z = 0.127$ km, over the interval $2 \leq t \leq 6$ h. Stippled regions enclose vertical vorticity values greater than or equal to 0.008 s^{-1}. The bold gray line indicates the -1-K perturbation temperature isotherm. Only a 100 km $\times$ 100 km portion of the full domain is shown.

5. Association with damaging, near-ground winds

One implication of the low-level mesovortices simulated herein is their tendency to be associated with strong winds, which we assert would be manifested in hypothetical "straight line" damage patterns (e.g., Fujita 1978; Forbes and Wakimoto 1983), considering the asymmetry and breadth of the vortices. In the following, we investigate mesovortex-associated "damaging" winds and also compare such to damaging, convectively produced winds often found at the apex of the bow echo (Fujita 1978, 1979).

Consistent with the conceptual models of Fujita (1978, 1979), a plot of the magnitude of the ground-relative horizontal winds[4] (V_{GR}) at $z = 127$ m and $t = 5$ h shows a kilometer-wide strip of $V_{GR} \geq 30$ m s^{-1} just behind the gust front at the primary bow-echo apex (Fig. 16a); these winds are due to descending rear inflow and its accompanying high perturbation pressure. More prominent in this figure, however, is the broad area of $V_{GR} \geq 30$ m s^{-1} that encompasses the two 35 m s^{-1} wind maxima associated with the south-southwest flanks of vortices BEV1 and BEV2.[5] Such a mesovortex–high-wind association is maintained during the interval $2 \leq t \leq 6$ h (Fig. 17) and, moreover, explains the increase

FIG. 16. Horizontal cross section, at $z = 0.127$ km, of horizontal velocity vectors, *ground-relative* horizontal wind magnitude, and pressure perturbation, at $t = 5$ h, for the (a) 20/2.5/f and (b) 20/2.5/0 experiments. The gray line in (a) indicates the trajectory discussed in the text. Horizontal wind magnitude values greater than 35 m s^{-1} have dark shading and those between 30 and 35 m s^{-1} have light shading. Pressure contour interval is 0.5 mb. Every second vector is plotted, and the vector length is scaled so that a distance of two grid lengths represents a vector magnitude of 10 m s^{-1}. Asterisks indicate time-series locations at 5 h. Only a 40 km $\times$ 40 km portion of the full domain is shown.

real atmosphere, however, environments of mesoconvective systems may contain inhomogeneities, such as surface outflow boundaries, that possess horizontal shear. Thus, in these instances the dominance of the mesovortexgenesis mechanism described above over that involving a horizontal shearing instability would depend on the characteristics of the horizontal shear.
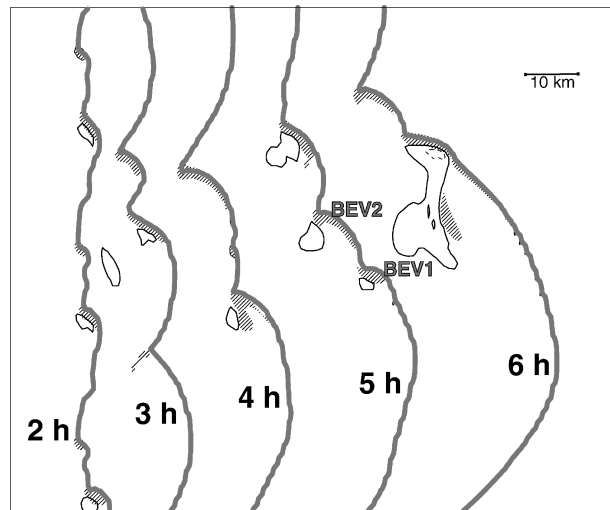
---

[4] Ground-relative winds are obtained by adding back in the constant velocity (18.0 m s^{-1}, -2.0 m s^{-1}) initially subtracted from the model winds (Part I). We note that the quantitative wind speeds (as presented in this section) should not be interpreted literally to represent those found at the earth's surface, since the lowest grid level for horizontal winds is at $z = 127$ m and also since a free-slip condition is applied to the bottom boundary.

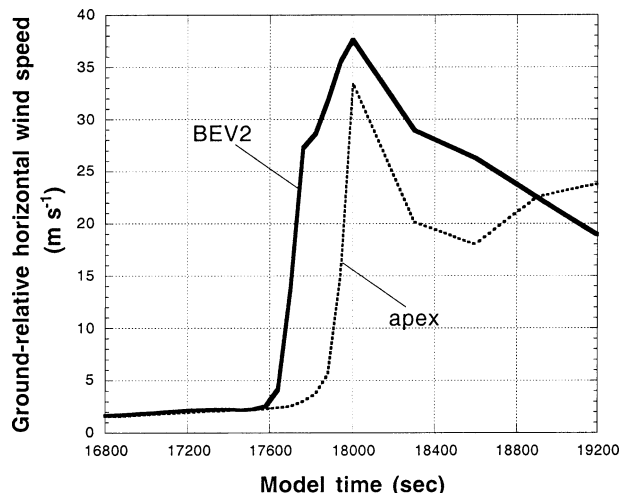[5] BEV1 and BEV2 are labeled V4 and V6, respectively, in Fig. 7 of Part I.

FIG. 18. Time series of ground-relative wind (m s^{-1}) at ground-fixed points affected by BEV2 and the bow-echo apex at $t = 5$ h (see Fig. 16).

TABLE 1. Area ($\times 10^7$ m^2) within specified isotach of ground-relative wind speed, as a function of system-relative location (see text) and model time (left column, $t = 5$ h; right column, $t = 6$ h). Wind data are from the $U_s = 20/2.5/f$ case, at the lowest grid level ($z = 127$ m).

Isotach value (m s^{-1})	BEV1–BEV2		Apex	
30	18.8	40.8	1.3	1.8
35	1.9	12.5	0.0	0.0
40	0.0	0.2	0.0	0.0

with time in the areal extent of strong winds. For example, the large area enclosed by the 35 m s^{-1} isotach at $t = 6$ h can be related to an amalgamation of BEV1 and BEV2. We can contrast this evolution with that in the 20/2.5/0 simulation, which is a ''control'' case of sorts, owing to its lack of significant low-level mesovortices. Correspondingly, high wind speeds can be found at low levels only in a narrow zone behind the gust front (Fig. 16b).

One may infer from the preceding paragraph that in the 20/2.5/f simulation, near-ground winds at the bow-echo apex can be less damaging than those with the mesovortices. Quantified in terms of local wind duration, this inference is correct: at a point fixed at the ground and affected by BEV2 (see Fig. 16a), ground-relative winds are greater than or equal to 30 (35) m s^{-1} for 402 (162) s, during the 40-min period centered at $t = 5$ h (Fig. 18). In contrast, at a point affected by the bow-echo apex, ground-relative winds are greater than or equal to 30 m s^{-1} for 78 s (Fig. 18). Additional quantitative confirmation is given in Table 1, which indicates that at $t = 5$ h the horizontal area encompassing the $V_{GR} = 30$ m s^{-1} isotach associated with BEV1 and BEV2 is an order of magnitude larger than that in the vicinity of the apex (see also Fig. 16a); an even larger difference in this areal extent of damaging winds with respect to the two system-relative locations is found at $t = 6$ h (and also for $V_{GR} \geq 35$ m s^{-1}; Table 1).

Observational data that corroborate our model results can be found in Miller and Johns (2000). They show, for example, that in the case of the mesoscale convective system of 4 July 1999, a large blowdown of trees ''occurred underneath the northern part of the storm complex—*not* the rapidly bowing southern section,'' and add that wind damage ''along the path of the very intense bow echo is not nearly as widespread and has only pockets of very severe damage.'' The attribution by

Miller and Johns of the widespread severe-wind damage to embedded high-precipitation supercell storms and the review by Seimon (1998) of ''devastating windstorms'' owing to supercell mesocyclones at the surface motivates the following analysis in which we seek to determine the forcing of what have been labeled thus far as mesovortex-*associated* winds.

Consider the trajectory of a parcel that populates the wind maximum at $t = 5$ h near BEV2 (e.g., Fig. 16a). The trajectory originates 20 min prior in a location ~ 15 km to the northwest and at an altitude generally less than or equal to 1 km (e.g., Fig. 19a). Its rate of descent from this altitude never exceeds 2 m s^{-1}; a similar conclusion can be reached for eight other parcels in the vicinity of BEV2. Hence, we can rule out the possibility that locally intense downdrafts or downbursts are responsible for the large V_{GR} near the mesovortices. The other, perhaps more apparent possibility based on the pressure field in Fig. 16a is that the damaging winds are driven by the low pressure, hence large horizontal pressure gradients, induced by the mesovortices. The following analysis of the pressure-gradient forcing of horizontal momentum along the trajectory allows an evaluation of this hypothesis.

Perturbation pressure π can be decomposed, as in Rotunno and Klemp (1985), into contributions from ''buoyancy'' (B) (π_B) and ''dynamics'' (π_{DN}), where

$$\nabla \cdot (c_p \overline{\rho} \overline{\theta} \nabla \pi_B) = \frac{\partial B}{\partial z}, \quad \text{and} \tag{5.1a}$$

$$\nabla \cdot (c_p \overline{\rho} \overline{\theta} \nabla \pi_{DN}) = \frac{\overline{\rho}}{2} [\omega_i \omega_i] - \overline{\rho} [e_{ij} e_{ij}] + \overline{\rho} \left(\frac{d^2 \ln \overline{\rho}}{dz^2} w^2 \right), \tag{5.1b}$$

where, in tensor notation, ω_i is the 3D vorticity vector, e_{ij} is the 3D rate of strain tensor,

$$e_{ij} = \frac{1}{2} \left(\frac{\partial u_i}{\partial x_j} + \frac{\partial u_j}{\partial x_i} \right),$$

and all other variables have their traditional meanings. Of particular interest is the contribution to the dynamics pressure from the vertical component of vorticity squared [hereafter referred to as ''vorticity squared,'' $\pi_{\zeta\zeta}$; first term on the rhs of Eq. (5.1b), evaluated for $i = 3$], through which the effect of the mesovortices on
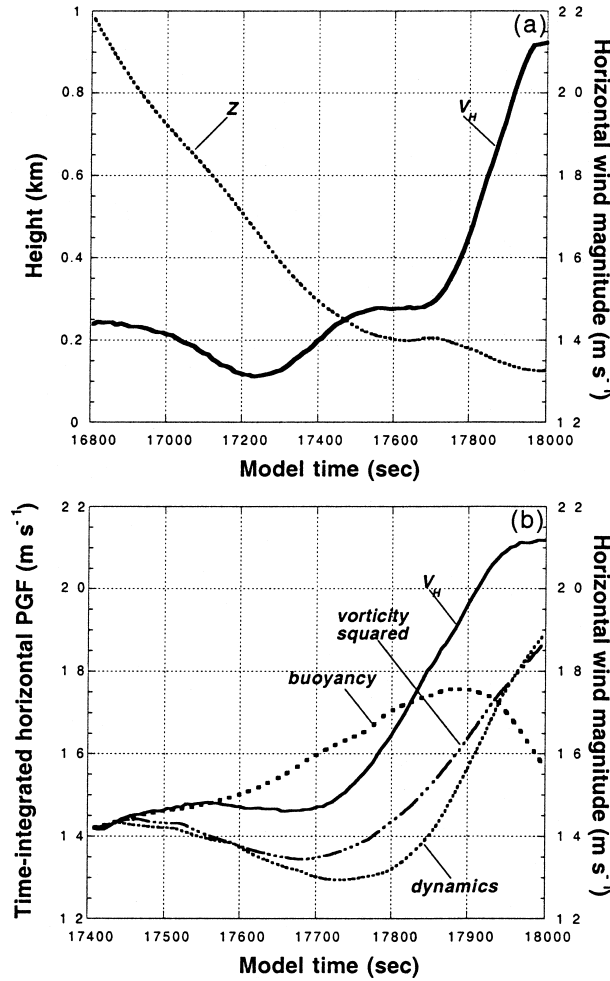
FIG. 19. (a) Time series of height [z (km); dotted line] and horizontal wind magnitude [V_H (m s^{-1}); solid line] along the trajectory indicated in Fig. 16. (b) Time series of V_H and of the time-integrated horizontal pressure-gradient force owing to "buoyancy" ($-c_p\overline{\theta}\partial\pi_B/\partial s$), "dynamics" ($-c_p\overline{\theta}\partial\pi_{DN}/\partial s$), and "vorticity squared" ($-c_p\overline{\theta}\partial\pi_{\zeta\zeta}/\partial s$) along part of the trajectory represented in (a). "Horizontal" here is the horizontal direction locally parallel to the trajectory (see text). Wind magnitude at t = 4 h 50 min is added to the time-integrated pressure-gradient force terms to allow for comparison with V_H. Note that the time domain of (b) is half that of (a).

the pressure field is represented. We compute the pressure-gradient force (HPGF) in the horizontal direction locally parallel to a trajectory,

$$-c_p\overline{\theta}\partial\pi_*/\partial s, \qquad (5.2)$$

where $\partial s = [(\partial x)^2 + (\partial y)^2]^{1/2}$, and then time integrate the HPGF owing separately to buoyancy, dynamics, and vorticity squared along all or part of the trajectory,

$$V_* = V_0 + \int_{t_0}^{t} \left(-c_p\overline{\theta}\frac{\partial\pi_*}{\partial s}\right) dt', \qquad (5.3)$$

where V_0 is the magnitude of the horizontal wind at time t_0, and * is the generic subscript for each of the three contributions.

During the interval 4 h 50 min $\leq t \leq$ 5 h, the parcel experiences a dramatic horizontal acceleration, at heights generally less than 0.2 km (Fig. 19a). Buoyancy forcing, or that associated directly with the cold pool, is responsible for most of the parcel acceleration until about a minute prior to t = 5 h; over the entire interval, however, the time-integrated buoyancy forcing contributes only 18% to the net gain in horizontal wind. In contrast, the contribution from $-c_p\overline{\theta}\partial\pi_{\zeta\zeta}/\partial s$ is initially small, at times well before the parcel is influenced by the vortex-induced low pressure. Over the entire period of integration, however, the integrated contribution amounts to more than three times that due to the cold-pool forcing. Clearly, the strongest low-level winds at this stage of the simulated QLCS are due largely to the low-level mesovortex circulations.

An obvious question at this point regards how well these conclusions can be generalized to QLCSs inhabiting environments with vertical wind profiles other than with U_S = 20 m s^{-1}/2.5 km. As demonstrated in Part I, significant, low-level mesovortices tend not to form within simulated QLCSs when the environment has weak low-level shear. Illustrating this result is the weak, upshear-tilted, effectively vortex-free QLCS produced in the 10/2.5/f experiment (Fig. 20a). Noteworthy, however, is the appearance of low-level winds with $V_{GR} \geq$ 30 m s^{-1} in a ~10 km wide band behind a bowing segment (Fig. 20b). Recalling the study by Weisman (1992), such a comparatively large area of strong surface winds trailing the convective system's leading edge is to be expected with an environmental shear of $U_S \sim$ 10 to 15 m s^{-1}/2.5 km (and with moderate environmental CAPE), owing to a resultant rear-inflow jet that descends and spreads laterally at the ground, well behind the gust front (Fig. 20b). In contrast, within environments of moderate-to-strong vertical wind shear (i.e., $U_S \geq$ 20 m s^{-1}/2.5 or 5 km in our model study) the RIJ tends to be elevated ~2–3 km above the ground; a branch of the rear inflow descends immediately behind the gust front, allowing only for a very thin strip of strong, post-frontal winds (Figs. 20c,d). Such environments also permit the formation of intense low-level mesovortices (see Part I) that, as just shown, can induce especially strong and damaging winds (Figs. 16a, 20d).

6. Effect on system structure and evolution

Intuition followed by close examination of the experimental results suggests that low-level mesovortices can also affect convective system structure and evolution. Case in point, the 20/2.5/f and 20/2.5/0 simulations have largely imperceptible differences at $t \sim$ 2 h, save for the respective presence and absence of developing low-level mesovortices (cf. Figs. 1a, 2a and Figs. 3a, 4a). At t = 3 h, however, we begin to find—exclusively in the 20/2.5/f simulation—the existence of pronounced horizontal undulations in the leading-edge updraft that by t = 4 h become updraft "fractures" (cf. Figs. 1b,c,
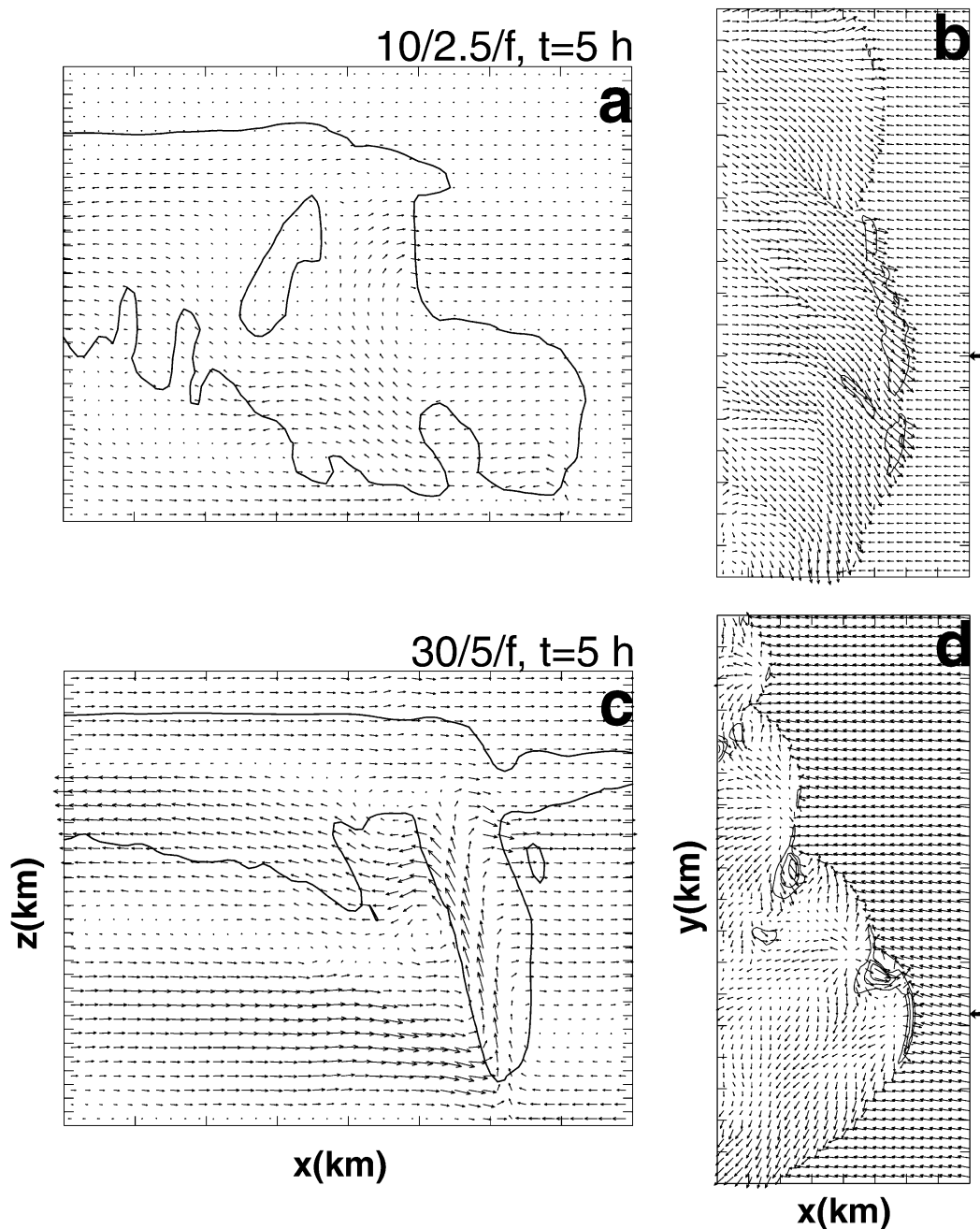
FIG. 20. Vertical and horizontal structure, at $t = 5$ h, of the convective systems simulated with (a), (b) $10/2.5/f$ and (c), (d) $30/5/f$. In (a) and (c), vertical cross sections of north–south-averaged [centered about $y = 70$ km and $y = 54$ km, respectively, as indicated in (b) and (d)] wind vectors and cloud water mixing ratio (0.1 g kg^{-1} contour) are presented. In (b) and (d), horizontal cross sections, at $z = 0.127$ km, of horizontal velocity vectors and the 30, 35, and 40 m s^{-1} contours of ground-relative horizontal wind magnitude are presented. Only an 80 km $\times$ 16 km (80 km $\times$ 180 km) portion of the full domain is shown in (a) and (c) [(b) and (d)].

2b,c and Figs. 3b,c, 4b,c). Such fractures span a considerable depth of the model troposphere, as can be visualized in a 3D rendering of vertical velocity (Fig. 21), and tend to be spatially correlated with low-level mesovortices such as BEV1 (see also Figs. 22a,b).

For more insight into this additional mesovortex im-

plication, we again turn to decompositions of pressure, expressed now in terms of $-c_p\overline{\theta}\partial\pi_B/\partial z + B$ and $-c_p\overline{\theta}\partial\pi_{DN}/\partial z$, the buoyancy forcing and dynamics forcing, respectively, of vertical momentum (Rotunno and Klemp 1982). During the mature stage of our modeled QLCS, we notice a dynamics-forcing minimum and
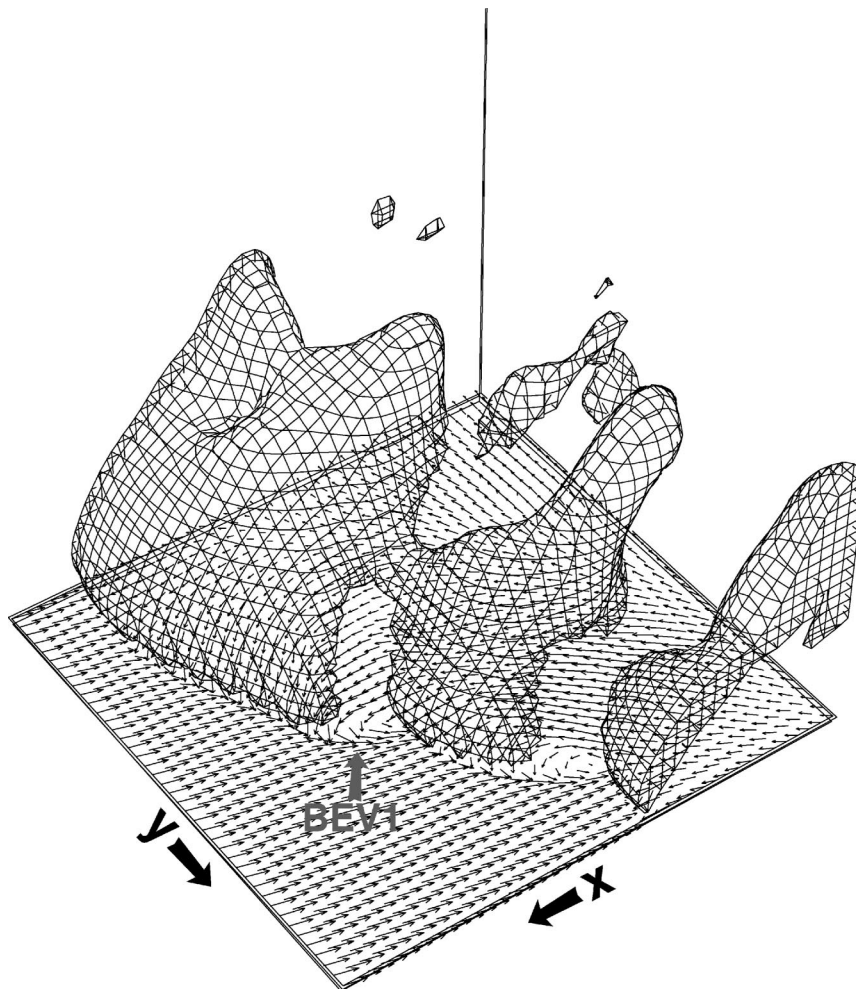
FIG. 21. Three-dimensional isosurface of vertical velocity and horizontal wind vectors, at $t = 5$ h. The isosurface value is 6 m s^{-1}. The vectors are plotted at $z = 0.25$ km, and the vector length is scaled so that a horizontal distance of 1 km represents a speed of 10 m s^{-1}. Only a 40 km $\times$ 40 km portion of the full domain in the horizontal directions is shown. The view is from the northeast.

maximum on the left and right flanks, respectively, of BEV1 and BEV2 at $z = 3$ km (Fig. 22c). These dynamics-forcing couplets can be attributed to the vertical tilt toward the south-southwest of the vortices and to the low pressure they induce. Hence, as alluded to in Fig. 21, a low-level mesovortex tends to reduce the midlevel (but also low-level; e.g., Fig. 22b) updraft at the system's leading edge; a mesovortex aloft tends to increase midlevel updraft behind the system's leading edge, although such an increase is offset by the negative buoyancy forcing at midlevels (Fig. 22d) associated with negatively buoyant air within the cold pool. The net effect is an absence of updraft above the low-level vortex position. Over time, this translates into a breakup or segmentation of the previously (nearly) continuous convective line, with new midlevel vortices often forming at the ends of the new segments, through the means described by WD98 and additionally through upward

advection of low-level mesovortex vorticity (see also Part I).

7. Summary and conclusions

Using a numerical cloud model, we have simulated long-lived quasi-linear mesoconvective systems (QLCSs) that possess significant, low-level meso-γ-scale vortices. We analyzed in detail an experiment with a model base-state CAPE of 2200 J kg^{-1} and unidirectional wind shear of 20 m s^{-1} over a surface-based depth of 2.5 km; this is an environment supportive of a squall line that develops strongly bowed segments. Sensitivity of low-level QLCS structure to environmental wind shear was discussed extensively in Part I (Weisman and Trapp 2003), which otherwise supports the robustness of the general results. The experiments and analyses of the current study have gained us fundamental insight
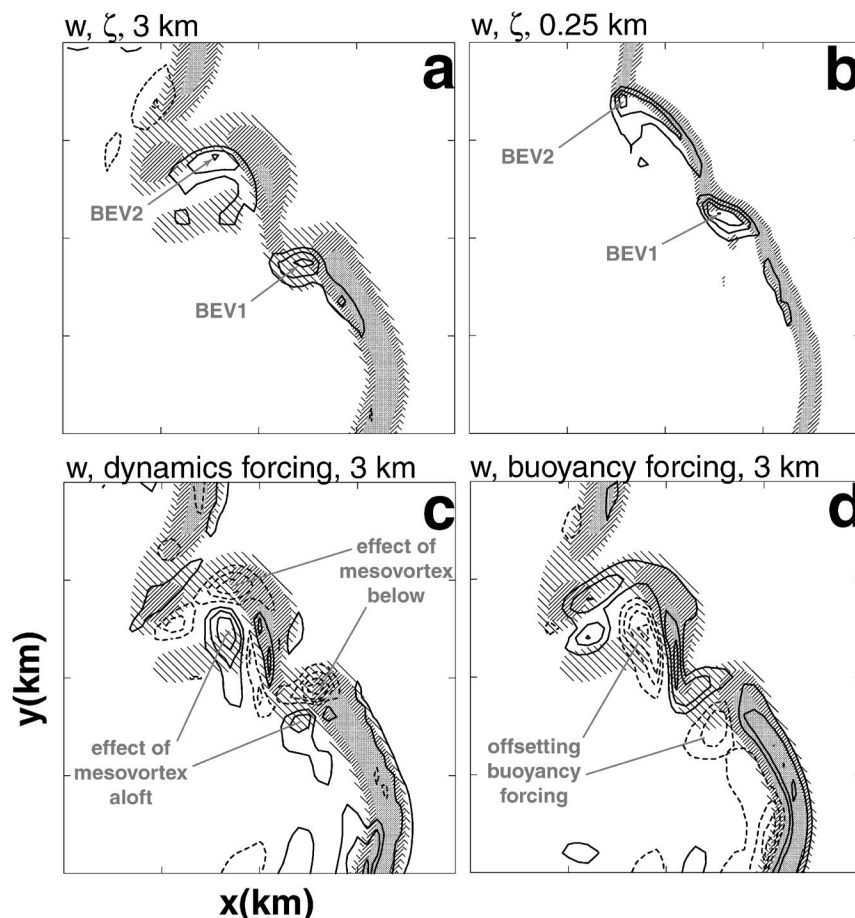
FIG. 22. Horizontal cross section, valid at $t = 5$ h, of vertical velocity and (a) vertical vorticity (contour interval 0.005 s^{-1}) at $z = 3.0$ km, (b) vertical vorticity (contour interval 0.005 s^{-1}) at $z = 0.25$ km, (c) dynamics forcing ($-c_p\overline{\theta}\partial\pi_{DN}/\partial z$; contour interval 0.001 m s^{-2}) at $z = 3.0$ km, and (d) buoyancy forcing ($-c_p\overline{\theta}\partial\pi_B/\partial z + B$; contour interval 0.001 m s^{-2}) at $z = 3.0$ km. In (a), (c), and (d), vertical velocity is lightly hatched for values between 2.5 and 5 m s^{-1}, heavily hatched for values between 5 and 10 m s^{-1}, and stippled for values greater than or equal to 10 m s^{-1}. In (b), vertical velocity is hatched for values between 1 and 2.5 m s^{-1} and stippled for values greater than or equal to 2.5 m s^{-1}. Only a 40 km $\times$ 40 km portion of the full domain is shown.

into the genesis and implications of low-level meso-vortices in QLCSs.

The mesovortices are generated just behind the leading-edge gust front of the QLCS, initially anywhere in the along-system direction. Once the QLCS becomes predominantly bow shaped, a northern bias in vortex location develops in the along-system direction. At all QLCS stages, most of the prominent low-level vortices rotate *cyclonically*. At all stages of a QLCS simulated without Coriolis forcing, low-level vortices tend not to be prominent, regardless of rotational sense.

Mesovortexgenesis is initiated at low levels by the tilting, in downdrafts, of initially crosswise baroclinic horizontal vorticity (Fig. 23); such horizontal vorticity may be associated with an RIJ (mature QLCS) or the cool outflow of a rainy downdraft (developing QLCS). Over a period of less than an hour, the symmetrical vortex couplet that results from tilting gives way to a dominant cyclonic vortex as the relative and, more notably, planetary vorticity is stretched vertically: hence, the Coriolis force plays a *direct* role in the genesis of low-level, cyclonic mesovortices and also in the mitigation of low-level, anticyclonic mesovortexgenesis. This proposed mechanism is different from that of supercellular low-level mesocyclogenesis vis-à-vis (i) the role of planetary vorticity (necessary and direct) and (ii) the velocity-vector relative orientation of the predominant horizontal vorticity (crosswise rather than streamwise) that is vertically tilted. Regarding (ii), the predominance of streamwise horizontal vorticity at low levels in supercells equates to an immediate formation of cyclonic low-level mesocyclones (e.g., see Fig. 9 of Davies-Jones and Brooks 1993), without the need of a symmetry- or vortex-couplet-breaking mechanism like
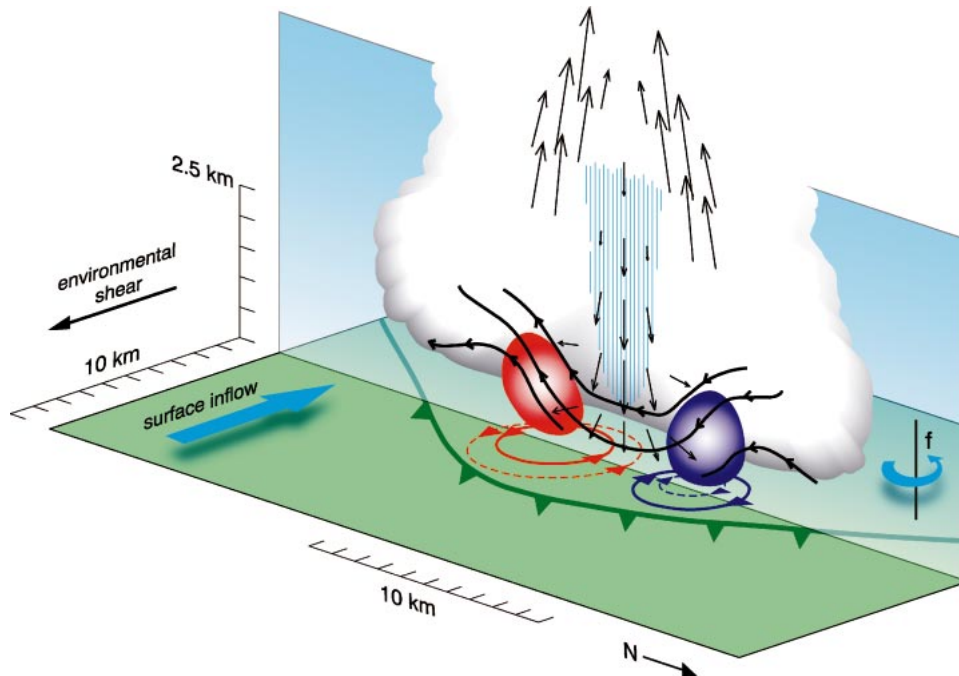
FIG. 23. Schematic showing a proposed mechanism for low-level mesovortexgenesis within a QLCS. The green barbed line indicates the gust front, vectors are of air motion in the vertical plane, blue hatching depicts rain core, bold black lines are vortex lines in the vertical plane, and red (purple) areas indicate positive (negative) vertical vorticity in the vertical plane. Vortex lines are tilted vertically by the downdraft, resulting in a surface vortex couplet (red is cyclonic vortex; purple is anticyclonic vortex). The future state of the vortex couplet, which results in part from the stretching of planetary vorticity (f), is shown by the dashed red and purple circles. Schematic represents early-QLCS-stage vortexgenesis. During the mature QLCS stage, relevant vortex lines would have opposite orientation; hence, resultant vortex couplet orientation would be reversed.

the stretching of planetary vorticity. Note that such symmetry breaking in the real atmosphere would also involve the stretching of synoptic-scale relative vorticity (e.g., along cold fronts), which may be abundant in the environments in which mesoconvective systems form and/or evolve.

We emphasize here as in Part I that many of the mesovortices form first within the lowest several hundred meters above the ground and thereafter grow upward to result in a mesovortex that extends through midlevels. Hence, the *low-level* mesovortices need not be preceded by and form beneath a midlevel mesovortex. Conversely, the *midlevel* mesovortices need not precede and otherwise be associated with a low-level mesovortex.

Analyses of forcing terms in the vertical and horizontal momentum equations revealed two implications of the low-level mesovortices. The first is that downward-directed vertical pressure gradients induced by the vortices effectively segment the previously (nearly) continuous convective line (Fig. 24), with new midlevel vortices often forming at the ends of the new segments. The second represents a new paradigm, akin to that proposed for supercells by Seimon (1998), for damaging low-level wind production in bow echoes: quantified in

terms of duration and areal extent, the strongest low-level winds are found in association with mesovortices, several tens of kilometers to the northwest of the bow apex. Occurring with QLCSs in moderately to strongly sheared environments, such damaging "straight line" winds are driven by the large horizontal pressure gradients associated with the mesovortices and exist in addition to the less damaging winds due to descending rear inflow at the bow-echo apex (Fig. 24). Weakly sheared environments, in contrast, support QLCSs that lack significant mesovortices but that still can produce damaging surface winds via descending rear inflow.

Observations that can be compared with our model results are currently lacking but will be available following the Bow Echo and Mesoscale Convective Vortex (MCV) Experiment (BAMEX; Davis et al. 2001). Analyses of the high-resolution BAMEX datasets, used in conjunction with real-case simulations (e.g., Atkins and Arnott 2002), will be used to verify, test the generality of, and/or explore further the mesovortexgenesis mechanism and subsequent implications described herein.
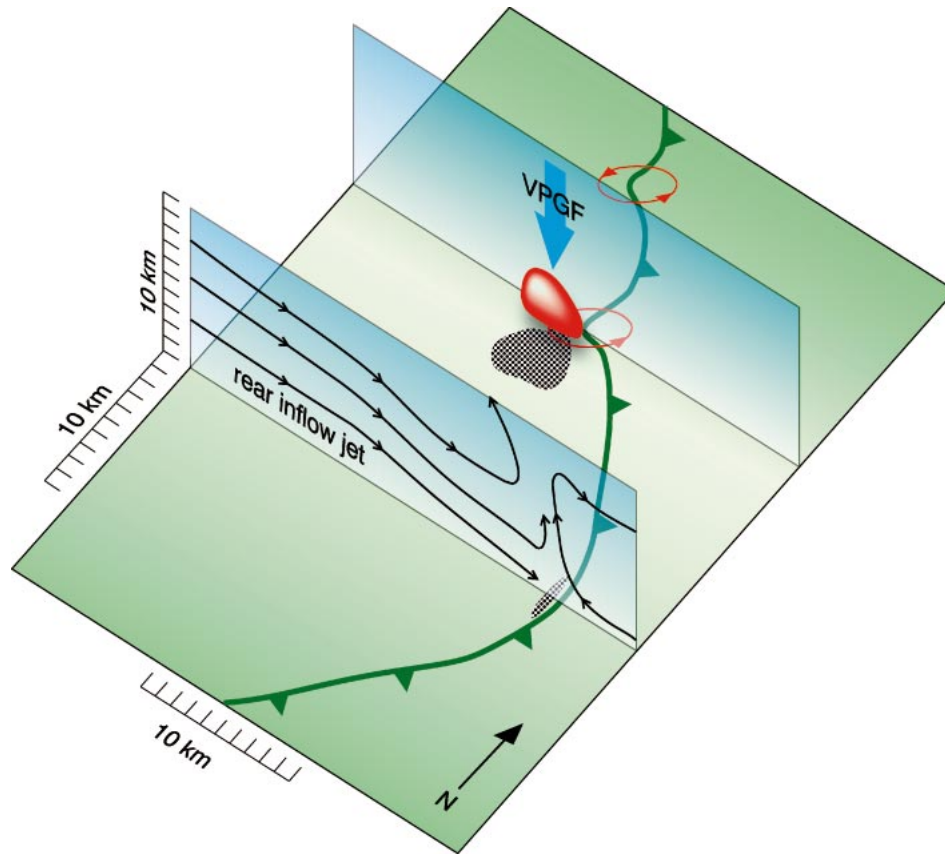
FIG. 24. Schematic showing proposed effect of low-level mesovortices on QLCS structure and also their role in the production of damaging surface winds. The green barbed line indicates gust front and red circles denote low-level mesovortices. The red area in the vertical plane shows vertical extent and tilt of positive vertical vorticity and the corresponding mesovortex. The implication is an associated downward-directed vertical pressure-gradient force (bold blue arrow) that acts to locally eliminate or ''fracture'' the updraft above the mesovortex location. Black stippling on the south-southwest flank of this mesovortex shows the area of instantaneous damaging ''straight line'' winds driven by the vortex circulation. A lesser area, or a narrow strip of such winds, is indicated well southeast of the vortex, at the apex of the primary bowing segment. These winds are due to a rear-inflow jet that descends to the ground, represented by the black streamlines in the other vertical plane.

REFERENCES

Atkins, N. T., and J. M. Arnott, 2002: Tornadogenesis within quasi-linear convective systems. Part II: Preliminary WRF simulation results of the 29 June 1998 derecho. Preprints, *21st Conf. on Severe Local Storms,* San Antonio, TX, Amer. Meteor. Soc., 498–501.

Bartels, D. L., and R. A. Maddox, 1991: Midlevel cyclonic vortices generated by mesoscale convective systems. *Mon. Wea. Rev.,* **119,** 104–118.

Carbone, R. E., 1983: A severe frontal rainband. Part II: Tornado parent vortex circulation. *J. Atmos. Sci.,* **40,** 2639–2654.

Davies-Jones, R., 1986: Tornado dynamics. *Thunderstorm Morphology and Dynamics,* 2d ed. E. Kessler, Ed., University of Oklahoma Press, 197–236.

——, 2000a: Can the hook echo instigate tornadogenesis barotropically? Preprints, *20th Conf. on Severe Local Storms,* Orlando, FL, Amer. Meteor. Soc., 269–272.

——, 2000b: A Lagrangian model for baroclinic genesis of mesoscale vortices. Part I: Theory. *J. Atmos. Sci.,* **57,** 715–736.

——, and H. E. Brooks, 1993: Mesocyclogenesis from a theoretical perspective. *The Tornado: Its Structure, Dynamics, Prediction, and Hazards, Geophys. Monogr.,* No. 79, Amer. Geophys. Union, 105–114.

——, R. J. Trapp, and H. B. Bluestein, 2001: Tornadoes and tornadic storms. *Severe Convective Storms, Meteor. Monogr.,* No. 50, Amer. Meteor. Soc., 167–222.

Davis, C. A., and Coauthors, cited 2001: Science overview of the bow echo and MCV experiment (BAMEX). [Available online at http://www.mmm.ucar.edu/bamex/science.html.]

Dutton, J. A., 1986: *The Ceaseless Wind.* McGraw-Hill, 617 pp.

Forbes, G. S., and R. M. Wakimoto, 1983: A concentrated outbreak of tornadoes, downbursts and mircobursts, and implications regarding vortex classification. *Mon. Wea. Rev.,* **111,** 220–235.

Fujita, T. T., 1978: Manual of downburst identification for project Nimrod. Satellite and Mesometeorology Research Paper 156, Dept. of Geophysical Sciences, University of Chicago, 104 pp. [NTIS PB-286048.]

——, 1979: Objectives, operation, and results of Project NIMROD. Preprints, *11th Conf. on Severe Local Storms,* Kansas City, MO, Amer. Meteor. Soc., 259–266.

——, 1981: Tornadoes and downbursts in the context of generalized planetary scales. *J. Atmos. Sci.,* **38,** 1511–1524.

Klemp, J. B., and R. B. Wilhelmson, 1978: The simulation of three-dimensional convective storm dynamics. *J. Atmos. Sci.,* **35,** 1070–1096.

——, and R. Rotunno, 1983: A study of the tornadic region within a supercell thunderstorm. *J. Atmos. Sci.,* **40,** 359–377.

Klimowski, B. A., R. Przybylinski, G. Schmocker, and M. R. Hjelmfelt, 2000: Observations of the formation and early evolution of bow echos. Preprints, *20th Conf. on Severe Local Storms,* Orlando, FL, Amer. Meteor. Soc., 44–47.

Lafore, J., and M. W. Moncrieff, 1989: A numerical investigation of the organization and interaction of the convective and stratiform regions of tropical squall lines. *J. Atmos. Sci.,* **46,** 521–544.

Lee, B. D., and R. B. Wilhelmson, 1997: The numerical simulation of non-supercell tornadogenesis. Part I: Initiation and evolution of pretornadic misocyclone and circulations along a dry outflow boundary. *J. Atmos. Sci.,* **54,** 32–60.

Lilly, D. K., 1976: Sources of rotation and energy in the tornado. *Proc. Symp. on Tornadoes: Assessment of Knowledge and Implications for Man,* Lubbock, TX, Texas Tech University, 145–150.

Mak, M., 2001: Nonhydrostatic barotropic instability: Applicability to nonsupercell tornadogenesis. *J. Atmos. Sci.,* **58,** 1965–1977.

Miller, D. J., and R. H. Johns, 2000: A detailed look at extreme wind damage in derecho events. Preprints, *20th Conf. on Severe Local Storms,* Orlando, FL, Amer. Meteor. Soc., 52–55.

Orlanksi, I., 1975: A rational subdivision of scales for atmospheric processes. *Bull. Amer. Meteor. Soc.,* **56,** 527–530.

Przybylinski, R. W., 1995: The bow echo: Observations, numerical simulations, and severe weather detection methods. *Wea. Forecasting,* **10,** 203–218.

Rotunno, R., and J. B. Klemp, 1982: The influence of the shear-induced pressure gradient on thunderstorm motion. *Mon. Wea. Rev.,* **110,** 136–151.

——, and ——, 1985: On the rotation and propagation of simulated supercell thunderstorms. *J. Atmos. Sci.,* **42,** 463–485.

——, ——, and M. L. Weisman, 1988: A theory for strong, long-lived squall lines. *J. Atmos. Sci.,* **46,** 463–485.

Schmidt, J. M., and W. R. Cotton, 1989: A High Plains squall line associated with severe surface winds. *J. Atmos. Sci.,* **46,** 281–302.

Seimon, A., 1998: Devastating mesocyclonic windstorms. Preprints, *19th Conf. on Severe Local Storms,* Minneapolis, MN, Amer. Meteor. Soc., 448.

Skamarock, W. C., M. L. Weisman, and J. B. Klemp, 1994: Three-dimensional evolution of simulated long-lived squall lines. *J. Atmos. Sci.,* **51,** 2563–2584.

Smull, B. F., and R. A. Houze Jr., 1987: Rear inflow in squall lines with trailing stratiform precipitation. *Mon. Wea. Rev.,* **115,** 2869–2889.

Thorpe, A. J., M. J. Miller, and M. W. Moncrieff, 1982: Two-dimensional convection in non-constant shear: A model of mid-latitude squall lines. *Quart. J. Roy. Meteor. Soc.,* **108,** 739–762.

Trapp, R. J., and B. H. Fiedler, 1995: Tornado-like vortexgenesis in a simplified numerical model. *J. Atmos. Sci.,* **52,** 3757–3778.

Wakimoto, R. M., 1983: The West Bend, Wisconsin storm of 4 April 1981: A problem in operational meteorology. *J. Climate Appl. Meteor.,* **22,** 181–189.

——, 2001: Convectively driven high wind events. *Severe Convective Storms, Meteor. Monogr.,* No. 50, Amer. Meteor. Soc., 255–298.

——, C. Liu, and H. Cai, 1998: The Garden City, Kansas, storm during VORTEX 95. Part I: Overview of the storm's life cycle and mesocyclogenesis. *Mon. Wea. Rev.,* **126,** 372–392.

Weisman, M. L., 1992: The role of convectively generated rear-inflow jets in the evolution of long-lived mesoconvective systems. *J. Atmos. Sci.,* **49,** 1826–1847.

——, 1993: The genesis of severe, long-lived bow echoes. *J. Atmos. Sci.,* **50,** 645–670.

——, 2001: Bow echoes: A tribute to T. T. Fujita. *Bull. Amer. Meteor. Soc.,* **82,** 97–116.

——, and C. A. Davis, 1998: Mechanisms for the generation of mesoscale vortices within quasi-linear convective systems. *J. Atmos. Sci.,* **55,** 2603–2622.

——, and R. J. Trapp, 2003: Low-level mesovortices within squall lines and bow echoes. Part I: Overview and sensitivity to environmental vertical wind shear. *Mon. Wea. Rev.,* **131,** 2779–2803.

Wicker, L. J., and R. B. Wilhelmson, 1995: Simulation and analysis of tornado development and decay within a three-dimensional supercell thunderstorm. *J. Atmos. Sci.,* **52,** 2675–2703.